Title
An Equivalent Circuit Model for Tunable Bandpass Filters Based on Ferromagnetic Resonance

Author
Gao, Qian

Publication Date
2021

Peer reviewed|Thesis/dissertation

UNIVERSITY OF CALIFORNIA

Los Angeles

An Equivalent Circuit Model for Tunable Bandpass Filters Based on Ferromagnetic Resonance

A thesis submitted in partial satisfaction

of the requirements for the degree Master of Science

in Electrical & Computer Engineering

by

Qian Gao

2021

ABSTRACT OF THE THESIS

An Equivalent Circuit Model for Tunable Bandpass Filters Based on Ferromagnetic Resonance

by

Qian Gao

Master of Science in Electrical & Computer Engineering

University of California, Los Angeles, 2021

Professor Yuanxun Wang, Chair

An equivalent circuit model for transmission line loaded thin film ferrimagnetic material is proposed, which can be utilized to synthesize the bandpass filters. Theoretical derivation based on Landau-Lifshitz-Gilbert (LLG) equation and Kittel's equation is applied to model thin film ferrite as a parallel RLC resonator, whose resonant frequency is determined by the ferromagnetic resonance (FMR) frequency. The transmission line loaded thin film ferrite structure is simulated and the resultant impedances match with that obtained from equivalent circuit model by tuning the effective thickness of the ferrite. The ferrite resonators are utilized to construct the 3rd order bandpass filters at FMR frequency. The filter center frequency tunability is realized by changing the magnetic bias field strength while the relative bandwidth tuning is realized by changing the coupling coefficients. The $BaFe_{12}O_{19}$ (BaM) ferrite is considered, whose internal anisotropy magnetic field is able to increase the FMR frequency to millimeter wave band. The effects of ferrite thickness, conductor width and transmission line structure are included.

The thesis of Qian Gao is approved.

Kang Lung Wang

Gregory P. Carman

Yuanxun Wang, Committee Chair

University of California, Los Angeles

2021

TABLE OF CONTENTS

LIST OF FIGURES

LIST OF TABLES

ACKNOLEDGEMENTS

I would like to thank my advisor, Professor Yuanxun Wang, for his professional guidance, remarks, and support for this work. Professor Wang would always point out where I made mistakes and discussed the potential research directions with me. I still remember the first day I met him and he told me that don't hesitate to reach out for help. His passion for research and exploring new fields has always inspired me.

In addition, I would like to thank Professor Greg Carman and Professor Kang Lung Wang for reviewing and providing insights for this thesis. I'm very glad to have them serve as my committee members. And they both offered valuable feedback during my presentation of this work.

I also want to thank my lab mates, Ting Lu and Xiating Zou for their help and meaningful discussions during the past two years.

Lastly, I want to thank my dear family, especially my mother and father, for their unconditional love and support. Without your understanding, I would not be able to chase my dream abroad.

CHAPTER 1

Introduction

Microwave magnetic devices have had a major impact on the development of microwave technology. Specifically, the microwave band pass and band stop filters play important roles in RF transmitter and receiver circuits to select the desired signal frequency range and to suppress the noise. Specifically, magnetic notch filters have been fabricated based on the ferromagnetic resonance (FMR) absorption and magnetostatic wave excitation. The anisotropy magnetic field inside the hexaferrite is able to increase the filter operation frequency up to millimeter wave band, making the magnetic filter a promising candidate for the construction of bandpass or bandstop filters. However, there has no equivalent circuit model developed to delineate the interaction between the spin waves and the RF signals in the form of EM waves, making it difficult to synthesize the desired filter response.

1.1 Background and Motivation

Ferrimagnets having low RF loss are used in multiple passive microwave components. Ever since the demonstration of microwave Faraday rotation in ferrites by Hogan in 1952, a diverse range of microwave magnetic devices were investigated and developed, many of which have found critical applications in military and civilian arenas. Examples include circulators, isolators, phase shifters, filters, signal-to-noise enhancers and frequency selective limiters operating in a wide range of frequencies (1–100 GHz) [14][15]. However, many intrinsic operation mechanisms remain unclear, and the physics based equivalent circuit models are also lacked. H Cui *et al.* proposed a nonlinear circuit model for frequency-selective limiters that is able to predict the frequency selectivity behavior, time delay and nonlinear insertion loss that match with actual measurements [1]. Motivated by this

model, this work utilized the linear equivalent model for ferromagnetic resonance (FMR) to synthesize the bandpass filter.

1.2 Millimeter Wave Band Stop Filter Based on Ferromagnetic Resonance

Young-Yeal Song *et al.* demonstrated a hexagonal ferrite mm-wave filter that is based on a $BaFe_{12}O_{19}$ (BaM) slab with in-plane anisotropy [2]. Figure 1.2.1 (a) is a schematic diagram of the device structure. A BaM hexagonal ferrite thin slab is positioned on top of a stripline structure, with its in-plane c axis along the stripline. An external static magnetic field H is applied parallel to the c axis. The microwave magnetic field h produced by the stripline is to a large degree in the plane of the BaM slab and perpendicular to the c axis. The BaM slab has an in-plane uniaxial anisotropy field of 17 kOe. Figure 1.1.1 (b) shows the relationship between theoretical FMR frequency versus biasing field according to Kittel's equation [4]:

$$\omega_r = \mu_0\gamma\sqrt{(H + H_a + (N_x - N_z)M_s)(H + H_a + (N_y - N_z)M_s)} \qquad (1.2.1)$$

, where $\mu_0\gamma = 2\pi \times \frac{2.7GHz}{kOe}$, $N_x = 0.54,\ N_y = 0.16,\ N_z = 0.3$, $4\pi M_s = 4.3\ kG$. The high anisotropy field H_a facilitates high operation frequency with not so large biasing field. In addition, by virtue of the high anisotropy field, the FMR frequency has a linear relation with the static biasing field. The tunability of bandstop filter center frequency is achieved by changing the biasing field.

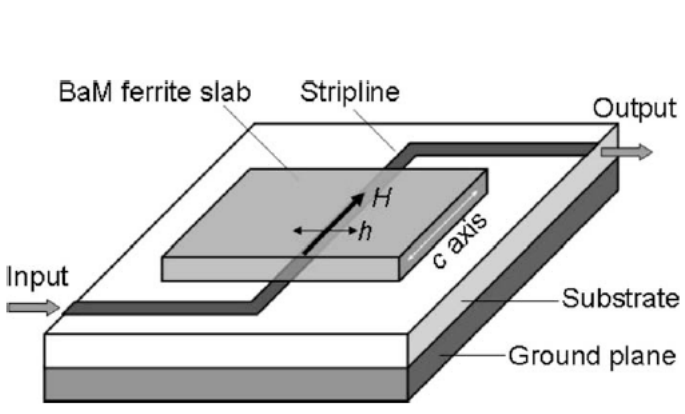

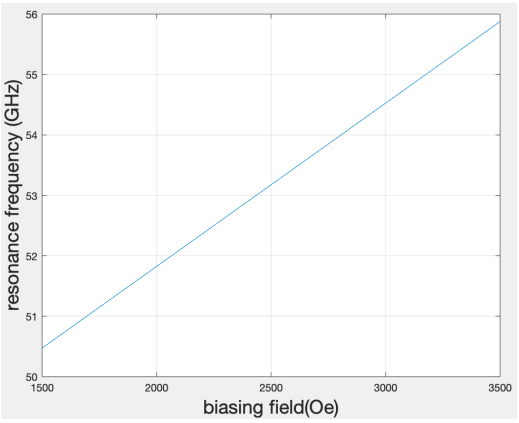

(a) (b)

Figure 1.2.1 (a) Schematic of BaM ferrite-based notch filter [2] (b) FMR frequency versus biasing field for BaM ferrite

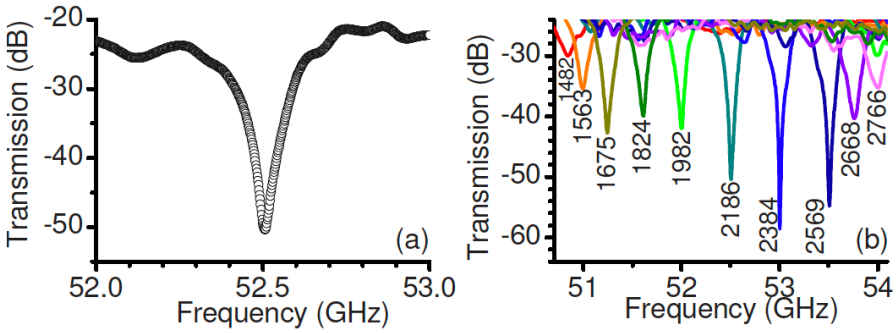

Figure 1.2.2 (a) Transmission coefficient vs frequency profile for H=2186 Oe (b) Transmission profiles for ten different fields [2]

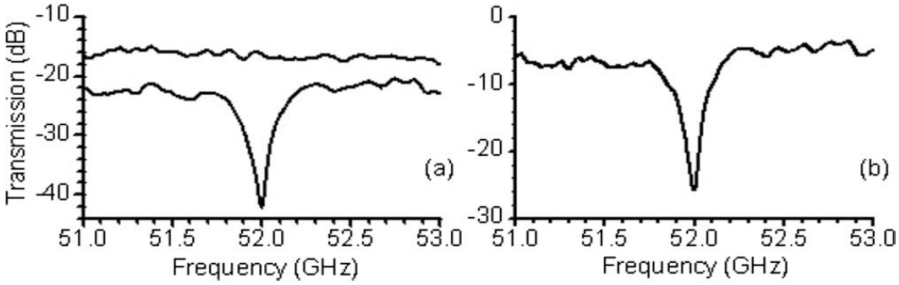

Figure 1.2.3 (a) Upper curve: transmission profile for the strip line structure only; Lower curve: transmission profile for the BaM slab/strip line structure under a field of 1982 Oe. (b) Difference between the lower and upper transmission profiles in (a). [2]

Figure 1.2.2 (a) demonstrates a band-stop response at 52.5 GHz, while Figure 1.2.2 (b) indicates that, through a change in the biasing field, one can shift the stop band over a frequency range. The band stop notches match with the theoretical FMR frequency that was calculated earlier. This confirms that the observed notch responses originate from the FMR absorption in the BaM slab. Figure 1.2.3 indicates that the maximum relative rejection is about 27 dB and the insertion loss of BaM slab is about 7 dB, which can be further minimized by better fabrication technique.

1.3 Millimeter Wave Band Stop Filter Based on Magnetostatic Wave Excitation

In addition to FMR absorption, Lu Lei *et al.* utilized magnetostatic wave excitation to construct notch filter [3]. The transmission line structure changed from stripline to co-planer waveguide (CPW) line because the alternating magnetic field produced by the CPW signal line is spatially nonuniform. And

this nonuniform field excites MSW modes in the BaM film, which is a kind of surface spin wave that propagates along the width direction. When width is small, confined MSWs are excited. The excitation of such modes leads to a low output power in a certain frequency range, namely, the band-stop filtering response, as shown in Figure 1.3.1. In addition, the MSW frequencies are higher than FMR frequency. The experimental filter notches frequencies agree with the theoretical MSW frequencies.

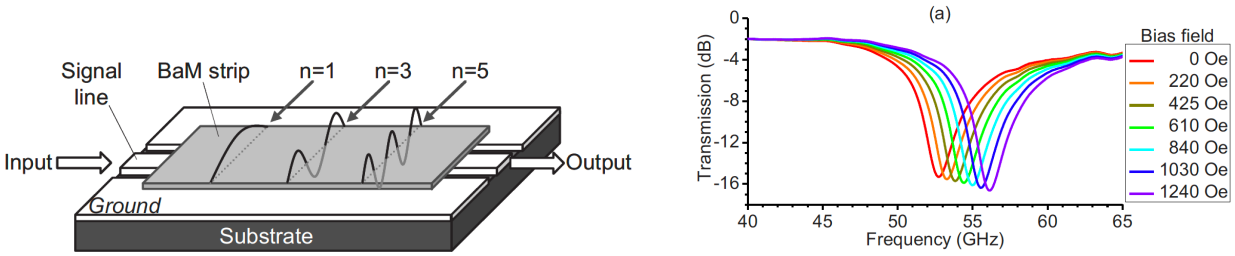

Figure 1.3.1 Diagram of a BaM notch filter and Transmission profiles for ten different fields [3]

1.4 Thesis Outline

In this work, an equivalent circuit model for magnetic bandpass filter is proposed. The theoretical derivation of the circuit model parameters is included in Chapter 2. The full wave (HFSS) and circuit (ADS) simulation results are presented and compared in Chapter 3. The match between the two sets of results validates the feasibility of the circuit model. In Chapter 4, the influences of several design parameters are discussed, including the ferrimagnetic material anisotropy field, ferrite thickness, conductor widths and transmission line structures. Chapter 5 concludes the thesis and points out future research directions.

CHAPTER 2

Equivalent Circuit Model of Tunable Bandpass Filter Based on FMR

In this chapter, we first introduce the ferromagnetic resonance (FMR) for ferrite material and calculate the FMR frequency for thin film ferrite based on Kittel's equation. Afterwards, the thin film ferrite is modeled as a parallel RLC resonator whose resonant frequency is the same as FMR frequency. In order to induce FMR, time varying magnetic field, i.e., RF field is generated by the transmission line structure. And the transmission line inductance is added to the previous circuit model. Finally, the transmission line loaded ferrite resonator is used to construct the 3rd order band pass filter.

2.1 Ferromagnetic Resonance of Thin Film Ferrite

In free space, the magnetic field intensity $\vec{H}$ is related with magnetic flux density $\vec{B}$ by the constitution relation:

$$\vec{B} = \mu_0 \vec{H} \tag{2.1.1}$$

, where $\mu_0 = 4\pi \times 10^{-7} H/m$ is the permeability of free space. However, in magnetic material, the application of external magnetic field $\vec{H}$ will change the polarization of the magnetic dipole. Depending on the reaction to the external field, magnetic material can be classified into various categories: paramagnetic, diamagnetic, ferromagnetic and ferrimagnetic. In the following discussion, we will limit our interest to ferrimagnetic material, in which the induced magnetic moment will align with the external magnetic field and increase the total magnetic flux in the material, as shown in Figure 2.1.1. In addition, the 'ferrite' is short for ferrimagnetic material.

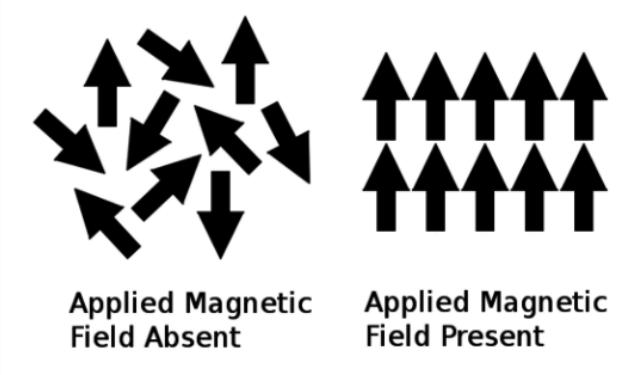

Figure 2.1. 1 The influence of external magnetic field on the magnetic dipole in ferrimagnetic material [16]

When a magnetic bias field $\overrightarrow{H_0} = \hat{z}H_0$ is present, a torque will be exerted on the magnetic dipole:

$$\vec{T} = \vec{m} \times \overrightarrow{B_0} = \mu_0 \vec{m} \times \overrightarrow{H_0} = -\mu_0 \gamma \vec{s} \times \overrightarrow{H_0} \tag{2.1.2}$$

And torque is equal to the time rate of change of angular momentum:

$$\vec{T} = \frac{d\vec{s}}{dt} = \frac{-1}{\gamma}\frac{d\vec{m}}{dt} = \mu_0 \vec{m} \times \overrightarrow{H_0} \tag{2.1.3}$$

Hence, the equation of motion for the magnetic dipole moment can be solved:

$$\frac{d\vec{m}}{dt} = -\mu_0 \gamma \vec{m} \times \overrightarrow{H_0} \tag{2.1.4}$$

Equation (2.1.4) can be decomposed into three scalar equations to solve for magnetization $\vec{m} = m_x\hat{x} + m_y\hat{y} + m_z\hat{z}$. And the solutions are:

$$m_x = Acos(\omega_o t), m_y = Asin(\omega_o t),\ \omega_0 = \mu_0 \gamma H_0 \tag{2.1.5}$$

, where ω_0 is called the *Larmor precession* frequency.

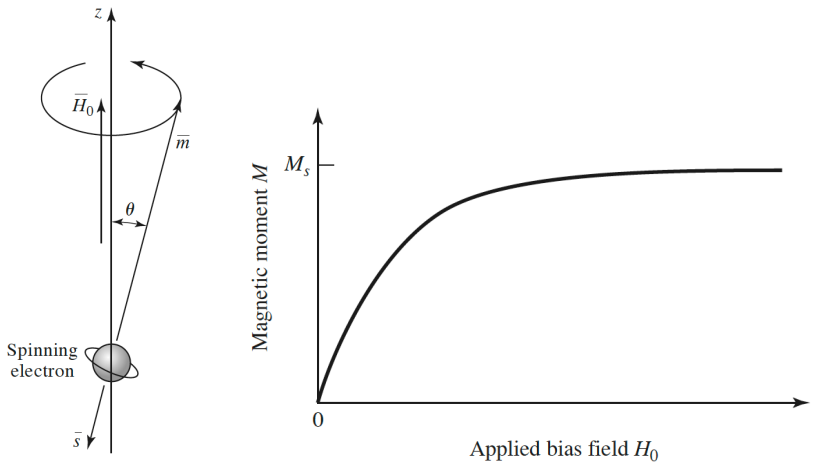

(a) (b)

Figure 2.1. 2 (a) Spin magnetic dipole and angular momentum vectors for a spinning electron (b) Magnetic moment of a ferrimagnetic material versus bias field H_0 [4]

The precession angle θ between $\vec{m}$ and z axis is given by

$$sin\theta = \frac{\sqrt{{m_x}^2+{m_y}^2}}{|\vec{m}|} = \frac{A}{|\vec{m}|} \tag{2.1.6}$$

Equation (2.1.5) indicates that $\vec{m}$ traces a circular path on the xy plane, and the precession frequency is ω_0. In the absence of damping force, the magnetic dipole will precess about H_0 indefinitely. However, in reality, the damping force will cause $\vec{m}$ to spiral in and finally align with H_0 [4].

Figure 2.1.1 (b) shows the relation between total magnetic moment in the ferrite versus the applied bias field. When the field strength increases, more magnetic dipole will be aligned, so the total magnetic moment will increase, until all the magnetic moments are aligned, and the ferrite is said to be magnetically saturated. M_s is the saturation magnetization, depending on the material properties.

When an additional small AC (microwave) magnetic field is added, it will interact with the magnetically saturated material and cause a forced precession of dipole moment at the frequency governed by the applied AC field. Let $\vec{H}$ be the applied AC field, the total magnetic field is:

$$\overrightarrow{H_t} = H_0\hat{z} + \vec{H} = H_0\hat{z} + H_x\hat{x} + H_y\hat{y} + H_z\hat{z} \tag{2.1.7}$$

, where $|\overrightarrow{H}| \ll H_0$. The total magnetization in the ferrite material is given by

$$\overrightarrow{M_t} = M_s\hat{z} + \vec{M} = M_s\hat{z} + M_x\hat{x} + M_y\hat{y} + M_z\hat{z} \tag{2.1.8}$$

And according LLG equation, $\frac{d\overrightarrow{M_t}}{dt} = -\mu_0\gamma\overrightarrow{M_t} \times \overrightarrow{H_t}$. Substituting (2.1.7) and (2.1.8) to the LLG equation and assuming AC $\vec{H}$ field has $e^{j\omega t}$ time dependence, $\vec{M}$ and $\vec{H}$ is related by the susceptibility tensor χ:

$$\vec{M} = [\chi]\vec{H} = \begin{bmatrix} \chi_{xx} & \chi_{xy} & 0 \\ \chi_{yx} & \chi_{yy} & 0 \\ 0 & 0 & 0 \end{bmatrix}\vec{H} \tag{2.1.9}$$

, where $\chi_{xx} = \chi_{yy} = \frac{\omega_0\omega_m}{{\omega_0}^2-\omega^2}, \chi_{xy} = -\chi_{yx} = \frac{j\omega\omega_m}{{\omega_0}^2-\omega^2}, \omega_0 = \mu_0\gamma H_0, \omega_m = \mu_0\gamma M_s.$

The magnetic flux density B and magnetic field intensity H is related:

$$\vec{B} = \mu_0\left(\vec{M} + \vec{H}\right) = [\mu]\vec{H} \tag{2.1.10}$$

Substituting (2.1.9) to (2.1.10), then the permeability tensor is derived to be

$$[\mu] = \mu_0([U] + [\chi]) = \begin{bmatrix} \mu & j\kappa & 0 \\ -j\kappa & \mu & 0 \\ 0 & 0 & \mu_0 \end{bmatrix} \tag{2.1.11}$$

, where $\mu = \mu_0(1 + \chi_{xx}) = \mu_0\left(1 + \frac{\omega_0\omega_m}{{\omega_0}^2-\omega^2}\right), \kappa = -j\mu_0\chi_{xy} = \frac{\mu_0\omega\omega_m}{{\omega_0}^2-\omega^2}$.

The physical meaning of permeability tensor $[\mu]$ is that it relates the AC magnetic field intensity with the induced magnetization in the ferrite material. Notably, from (2.1.9), when the AC field frequency ω is equal to the *Larmor precession* frequency ω_0, the denominator of the susceptibilities will vanish, indicating infinite induced magnetization. Of course, this will not happen in real world with loss present. However, this phenomenon is called gyromagnetic resonance or ferromagnetic resonance (FMR). And the FMR frequency is equal to the *Larmor precession* frequency ω_0 in infinite large ferrite samples. For a finite-sized ferrite sample, the FMR frequency is altered by the demagnetization factors, and is given by Kittel's equation [5]:

$$\omega_r = \sqrt{(\omega_0 + \omega_m N_x)(\omega_0 + \omega_m N_y)} \tag{2.1.12}$$

, where N_x, N_y is the demagnetization factors.

2.2 Equivalent Circuit Model for Thin Film Ferrite

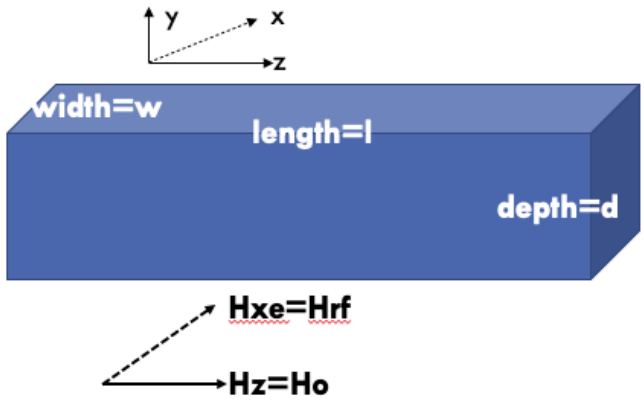

Figure 2.2.1: Diagram of thin film ferrite biased in z direction

In electrical circuits, RLC resonators can be used to characterize the resonant behavior in mechanical systems when two types of energy interact with each other. In ferrite material, the precession motion

of the magnetic dipole is analogies to the pendulum oscillation, where the magnetic energy and electric energy interact with each other during oscillation. At the highest position, the kinetic energy stored in the pendulum is zero, and the electric energy stored in the magnetic dipole is zero. At the lowest state of pendulum oscillation, the potential energy stored in the pendulum system is zero, and the magnetic energy stored in the magnetic dipole is zero, since the magnetic dipole is cutting the magnetic field lines at the largest speed, creating electric potential. The power loss in ferrite material is also present during magnetic moment precession, corresponding to the resistance in the RLC resonator. So intuitively, the magnetic dipole motion can be modeled by an RLC resonator, and the detailed derivation is attached below.

Figure 2.2.1 is the diagram of a thin film ferrite material, where the static bias magnetic field is applied in plane in z direction, and the AC magnetic field is perpendicular to the bias direction. The ferrite material thickness is assumed to be much smaller than the ferrite length and width and a complete demagnetization in thickness direction can be assumed, i.e., $N_y = 1$.

According to (2.1.9),

$$M_x = \chi_{xx} H_x + \chi_{xy} H_y \tag{2.2.1}$$

$$M_y = \chi_{yx} H_x + \chi_{yy} H_y \tag{2.2.2}$$

$$H_x = H_{xe} = H_{rf},\ H_y = H_{ye} - M_y \tag{2.2.3}$$

Note that (2.2.3) is valid since $N_y = 1$ is assumed. Substituting (2.2.3) to (2.2.1) and (2.2.2),

$$M_x = \frac{\chi_{xx} + \chi_{xx}\chi_{yy} - \chi_{xy}\chi_{yx}}{1+\chi_{yy}} H_{xe} + \frac{\chi_{xy}}{1+\chi_{yy}} H_{ye} \tag{2.2.4}$$

$$M_y = \frac{\chi_{yx}}{1+\chi_{yy}} H_{xe} + \frac{\chi_{yy}}{1+\chi_{yy}} H_{ye} \tag{2.2.5}$$

(2.2.4) and (2.2.5) give the relation between induced magnetization and the external applied magnetic field, influenced by the demagnetization factors. Hence, the effective susceptibilities can be defined:

$$M_x = \chi_{xxeff} H_{xe} + \chi_{xyeff} H_{ye} \tag{2.2.6}$$

$$M_y = \chi_{yxeff} H_{xe} + \chi_{yyeff} H_{ye} \tag{2.2.7}$$

Compare (2.2.6) with (2.2.4), then

$$\chi_{xxeff} = \frac{\chi_{xx}+\chi_{xx}\chi_{yy}-\chi_{xy}\chi_{yx}}{1+\chi_{yy}} \tag{2.2.8}$$

Substituting the expressions of χ_{xx}, χ_{xy}, χ_{yx}, and χ_{yy},

$$\chi_{xxeff} = \frac{\omega_m}{\omega_0} \frac{{\omega_r}^2}{{\omega_r}^2-\omega^2} \tag{2.2.9}$$

, where $\omega_r = \sqrt{\omega_0(\omega_0 + \omega_m)}$ is the resonant frequency of thin film ferrite calculated using Kittel's equation.

Similar to the RLC resonator, loss in the system can be included by making the resonant frequency complex:

$${\omega_r}^2 = (\omega_0 + j\alpha\omega)(\omega_m + \omega_0 + j\alpha\omega) \tag{2.2.10}$$

, where α is the Gilbert damping constant, depending on the type of ferrite material.

The impedance of the ferrite material can be derived from the external susceptibility:

$$Z_{eq\_ferrite} = j\omega\mu_0\chi_{xxeff}\frac{ld}{w} \tag{2.2.11}$$

Substituting (2.2.9) (2.2.10) to (2.2.11) and ignoring higher orders of α, the ferrite impedance can be mapped to the impedance of a parallel RLC resonator, where $Z_{RLC\_p} = \frac{1}{\frac{1}{Rm}+\frac{1}{j\omega Lm}+j\omega Cm}$ and

$$C_m = \frac{\omega_0}{\omega_r{}^2\mu_0\omega_m} \times \frac{w}{ld} \tag{2.2.12}$$

$$L_m = \frac{\mu_0\omega_m}{\omega_0} \times \frac{ld}{w} \tag{2.2.13}$$

$$R_m = \frac{\mu_0\omega_m\omega_r{}^2}{\alpha(2\omega_0+\omega_m)\omega_0} \times \frac{ld}{w} \tag{2.2.14}$$

2.3 Equivalent Circuit Model for Transmission Line Loaded Ferrite

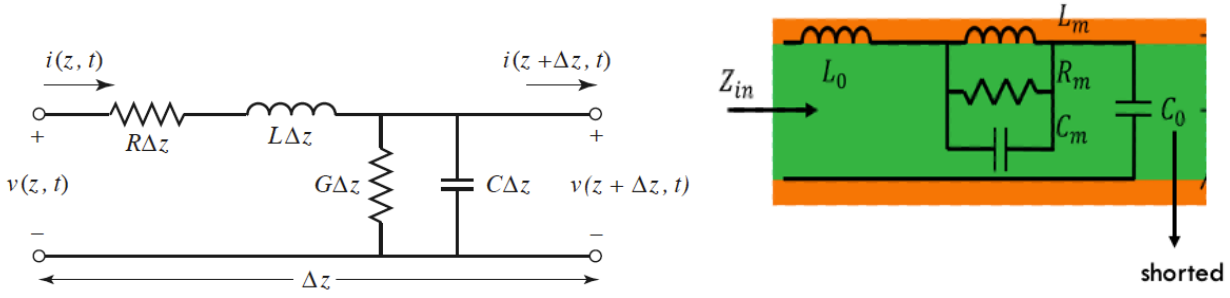

(a) (b)

Figure 2.3.1: (a) Lumped elements model of transmission line [4] (b) Equivalent circuit model of transmission line loaded ferrite material with L_0 representing shortened transmission line inductance [17]

In reality, the AC magnetic field exerted on the ferrite material is usually provided by the transmission line that guides the electromagnetic wave propagation. Hence, the parasitic of transmission line parameters must be taken into account to model the structure accurately. Figure 2.3.1(a) is the lumped elements model of transmission line, where R, L, G, C are the resistance,

inductance, conductance, and capacitance per unit length, respectively. Based on this equivalent circuit model, the input impedance of the transmission line with arbitrary load impedance Z_L can be derived. Specifically, when $Z_L = 0$, which means the transmission line is shortened at one end, the input impedance can be simplified:

$$Z_{TL} = jZ_o \tan \beta l \tag{2.3.1}$$

, where β is the propagation constant along the transmission line, l is the length of transmission line, and Z_0 is the characteristic impedance of the transmission line. When the length is much smaller than the wavelength, i.e., $\beta l \ll \frac{\pi}{2}$, $\tan \beta l \approx \beta l$. And Z_{TL} has a linear relationship with operating frequency, which can be viewed as a single inductor with equivalent inductance:

$$L_{TL} = \frac{Z_0}{v} \times l \tag{2.3.2}$$

Hence, when the bias field is applied perpendicular to the RF magnetic field generated by the transmission line, as shown in Figure 2.3.2, the total magnetic flux in the RF field direction will be greater with ferrite present, as indicated by (2.2.11). Hence, the transmission line inductor should have a series connection with the parallel RLC resonator representing such physics, as shown in Figure 2.3.1 (b), which is the equivalent circuit model of transmission line loaded ferrite structure when the transmission line length is much smaller than the EM wave wavelength and is shortened at one end.

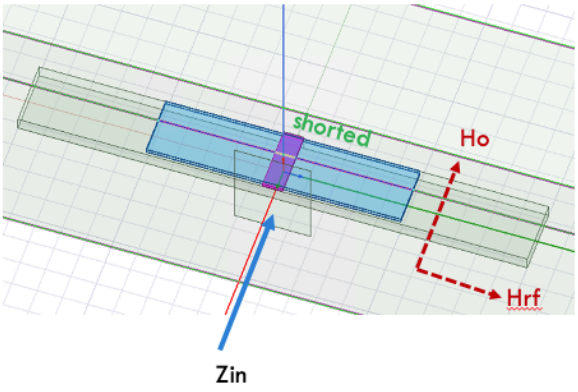

Figure 2.3.2: Schematic of transmission line loaded ferrite material

2.4 Equivalent Circuit Model for Bandpass Filter

Bandpass filters can be synthesized using the insertion loss method and implemented with the short-circuited transmission line stubs, as indicated in Figure 2.4.1 [4]. Quarter-wavelength sections of line between the stubs act as admittance inverters to effectively convert alternate shunt resonators to series resonators. The characteristic impedances of the shunt short-circuited transmission line stubs is given by:

$$Z_{on} = \frac{\pi Z_0 \Delta}{4 g_n} \tag{2.4.1}$$

, where Z_0 is the characteristic impedance of the quarter-wavelength sections, $\Delta = \frac{\omega_2 - \omega_1}{\omega_0}$ is the fractional bandwidth of the filter, and g_n is the low-pass prototype values.

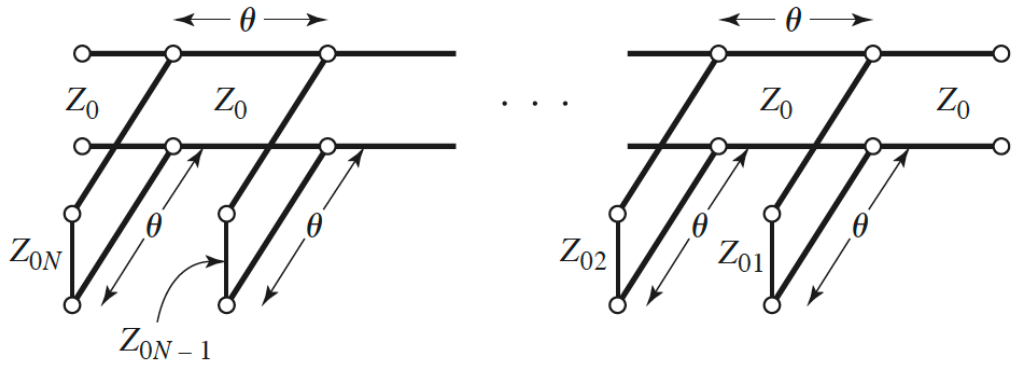

Figure 2.4.1: Bandpass filters using shunt transmission line resonators [4]

Afterwards, the short-circuited transmission line stubs are mapped to the parallel LC resonators, because it will be later represented by the circuit model of ferrite resonators, as shown in Figure 2.4.2. The input impedance of the short-circuited quarter wavelength transmission line near center frequency is:

$$Zin1 = jZ_0 tan\theta = \frac{-jZ_0}{tan\left(\frac{\pi\Delta\omega}{2\omega_0}\right)} \approx \frac{-jZ_0}{\left(\frac{\pi\Delta\omega}{2\omega_0}\right)} \tag{2.4.2}$$

And the input impedance of the LC resonator near center frequency is:

$$Zin2 = \frac{1}{\frac{1}{j\omega L_0} + j\omega C_0} = \frac{j\omega {L_0}{\omega_0}^2}{(\omega_0+\omega)(\omega_0-\omega)} \tag{2.4.3}$$

, where $\omega = \omega_0 + \Delta\omega$ and $\Delta\omega$ is some small deviation from center frequency. Equating $Zin1$ with $Zin2$, the L_0 and C_0 are found:

$$L_0 = \frac{4Z_0}{\pi\omega_0},\ C_0 = \frac{\pi}{4Z_0\omega_0} \tag{2.4.4}$$

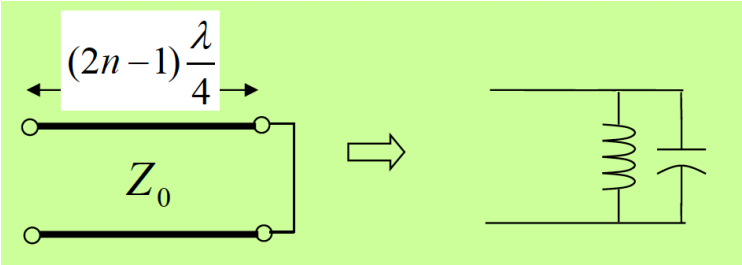

Figure 2.4.2: The equivalence of short-circuited quarter wavelength transmission line and parallel LC resonator [18]

Thus, the design procedure for bandpass filter is systematic. Firstly, the bandpass filter can be synthesized using the conventional coupled transmission line structure with the design equation given by (2.4.1). Afterwards, the shunt transmission line resonators are represented by the parallel LC resonators, and the desired LC values are calculated using (2.4.4). The ferrite resonator is used to construct these LC resonators, and the ferrite dimensions as well as the bias magnetic field strength can be derived using (2.2.12) to (2.2.14). In this way, the bandpass filter based on ferromagnetic resonance is synthesized. And the filter center frequency tuning can be easily implemented by changing bias magnetic field strength, as indicated in (2.1.9).

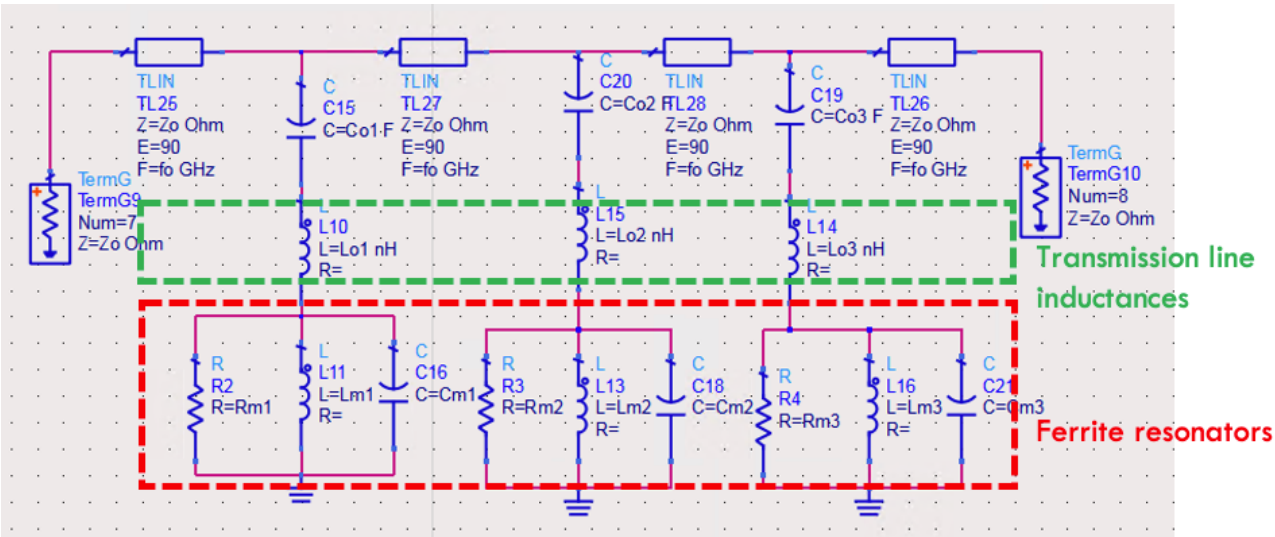

Figure 2.4.3: Equivalent circuit model for 3rd order bandpass filter using transmission line loaded ferrite resonators

The final equivalent circuit model of a 3rd order bandpass filter is shown in Figure 2.4.3. The $R_m, L_m,$ and C_m represent ferrite resonators whose resonant frequency (FMR frequency) is the same as the bandpass filter center frequency. $L_{o1}, L_{o2},$ and L_{o3} represent transmission line inductances given by (2.3.2). Since the effect of transmission line inductances are not included in the previous filter synthesize, the series C_{o1}, C_{o2}, and C_{o3} are added to cancel their effect to form series resonances at filter center frequency. However, the effect of $L_{o1}, L_{o2},$ and L_{o3} will become obvious when moving farer away from center frequency, which will be discussed in more details in the next two chapters.

CHAPTER 3

Design and Simulation of Tunable Bandpass Filters Based on FMR

In this chapter, we explain the detailed procedures of tunable bandpass filter synthesis using the proposed equivalent circuit model in Chapter 2. Firstly, the transmission line loaded ferrite structure is built in Ansys high-frequency structure simulator (HFSS) to facilitate full wave simulation for input impedances and resonance frequencies. Afterwards, the simulated S parameters are extracted and imported to Advanced Design System (ADS) to compare with the S parameters got from the circuit model. The close match between the two sets of results demonstrates the validity of the proposed circuit model. Afterwards, bandpass filter synthesis is performed using three resonators and the corresponding ferrite physical dimensions are derived. Finally, the bandpass filter center frequency tuning and relative bandwidth tuning are shown.

3.1 Construction of Stripline Loaded Ferrite in HFSS

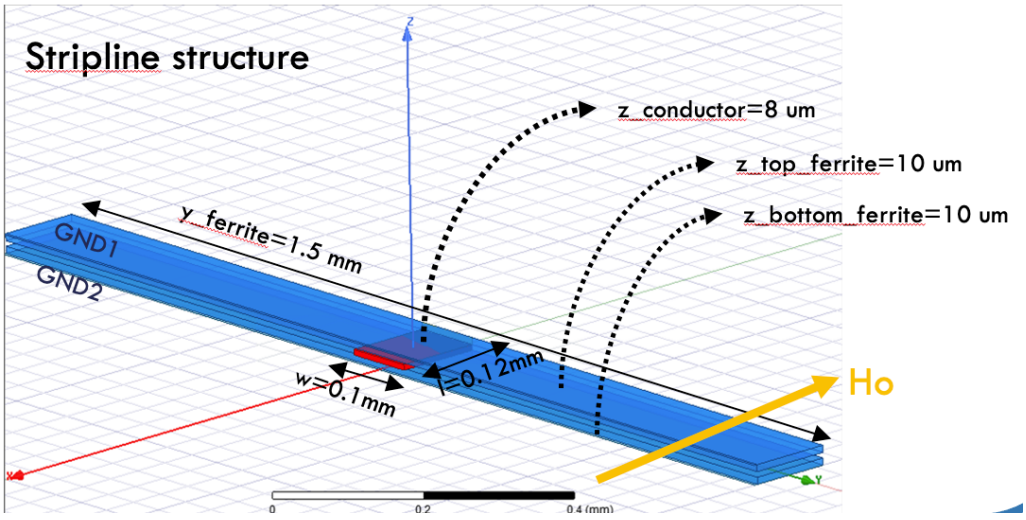

Figure 3.1.1: Modeling of stripline loaded ferrite in HFSS

Figure 3.1.1 illustrates the physical structure of the transmission line loaded ferrite resonator in HFSS. Specifically, stripline structure is exploited to provide the RF magnetic field that is perpendicular to the bias magnetic field. The comparison of stripline structure and microstrip line structure is included in Chapter 4. Compared with microstrip line structure, the stripline has the ground planes on both top and bottom. Thus, when two pieces of thin film ferrite materials are inserted between the center metal conductor and the ground planes, the RF magnetic field distribution is uniform across the ferrite material, exciting the ferromagnetic resonance (FMR) mode, which is the 0^{th} order spin wave mode [5]. Otherwise, higher order spin wave modes may be excited, which is not included in the proposed circuit model.

The choice of transmission line lengths, widths, and substrate thicknesses are optimized with respect to the frequency of operation. Since high frequency up to 30 GHz is considered, the corresponding wavelength is

$$\lambda = \frac{c}{f} = \frac{3\times10^8}{30\times10^9} m = 0.01m \tag{3.1.1}$$

, when air acts as the substrate. Hence, in order to use a single inductor to represent the transmission line, the length of the line should be smaller than $\frac{1}{10}\lambda = 1\ mm$. In this project, the length of the line varies between 0.1 mm to 0.2 mm to satisfy this requirement. And the transmission line inductance can be calculated from (2.3.1) and (2.3.2) and can be compared with the actual simulated results.

The width of transmission line is also an important parameter to optimize. On the one hand, the larger the width, the smaller the characteristic impedance of the transmission line itself, causing smaller transmission line inductance which is desirable since transmission line inductance is a parasitic in the ferrite resonators. On the other hand, larger widths will result in smaller ferrite inductance since

$L_m = \frac{\mu_0 \omega_m}{\omega_0} \times \frac{ld}{w}$ from (2.2.13). Thus, the width should be optimized to give a largest ratio between L_m and L_{TL}.

The substrates are filled entirely with ferrite material which has the thickness of 10 um. Thinner ferrite is required since the previous derivation assumed a complete demagnetization in the thickness direction. However, the ferrite can't be arbitrarily thin as well in order to give a reasonable L_m value.

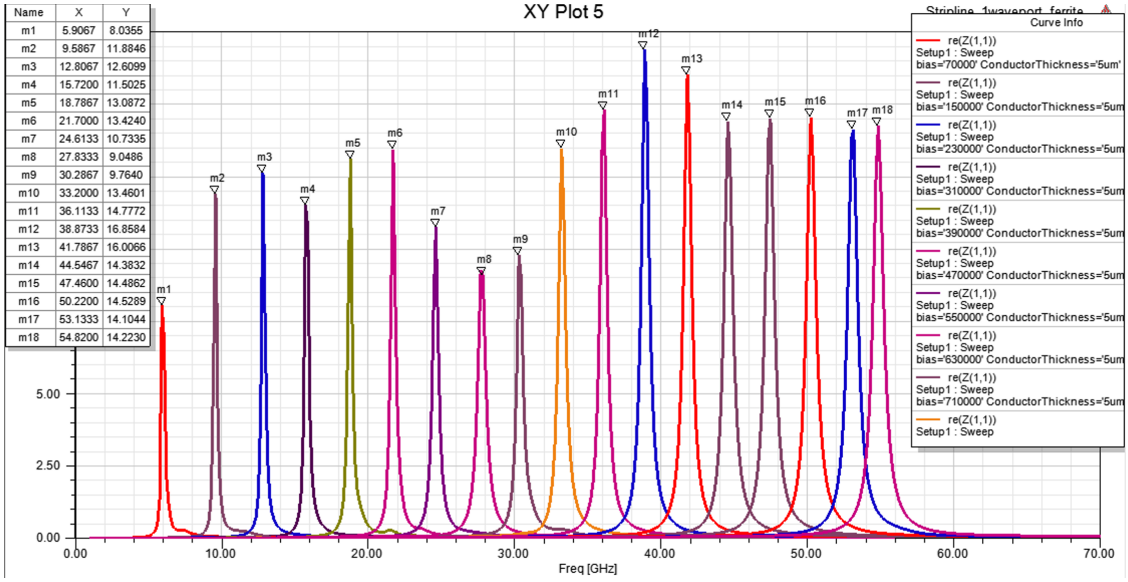

Figure 3.1.2: Real part of input impedances when sweeping bias magnetic field (plus internal anisotropy field) from 70000 A/m to 1400000 A/m with step 80000 A/m

Figure 3.1.2 shows the real part of input impedances when sweeping bias magnetic field from 70000 A/m to 1400000 A/m with step 80000 A/m. When the other end of transmission line is shorted, the input impedance is:

$$Z_{in} = Z_{TL} + Z_{ferrite} = j\omega L_{TL} + \frac{1}{\frac{1}{R_m} + \frac{1}{j\omega L_m} + j\omega C_m} \tag{3.1.2}$$

And at FMR frequency when $\frac{1}{j\omega L_m} + j\omega C_m = 0$, the real part on Z_{in} will reach the maximum. Hence, FMR frequencies can be extracted from the input impedances plot from HFSS. Figure 3.1.3 shows

the comparison between simulated FMR frequencies and theoretical FMR frequency given by Kittel's equation. The close match between the two indicates that FMR mode is excited in the ferrite material and the 10um thickness is thin enough to be considered thin film ferrite whose resonance frequency is given by $\omega_r = \sqrt{\omega_0(\omega_0 + \omega_m)}$ from (2.2.9).

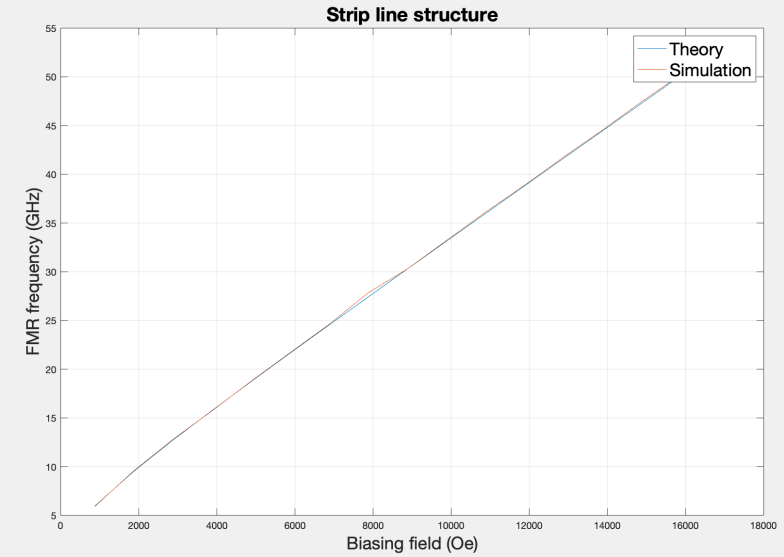

Figure 3.1.3: Comparison between simulated FMR frequency and theoretical FMR frequencies

3.2 Mapping HFSS results to equivalent circuit models

From the full wave simulation results got from HFSS, the validity of the proposed circuit model is tested. Figure 3.2.1 shows the simulation schematic in ADS to generate the input impedances plots for both cases. The SnP device represents the S parameter exported from HFSS. The upper circuit model is the proposed transmission line loaded ferrite resonator, where a parallel RLC resonator is in series with the transmission line inductance denoted as L_1.

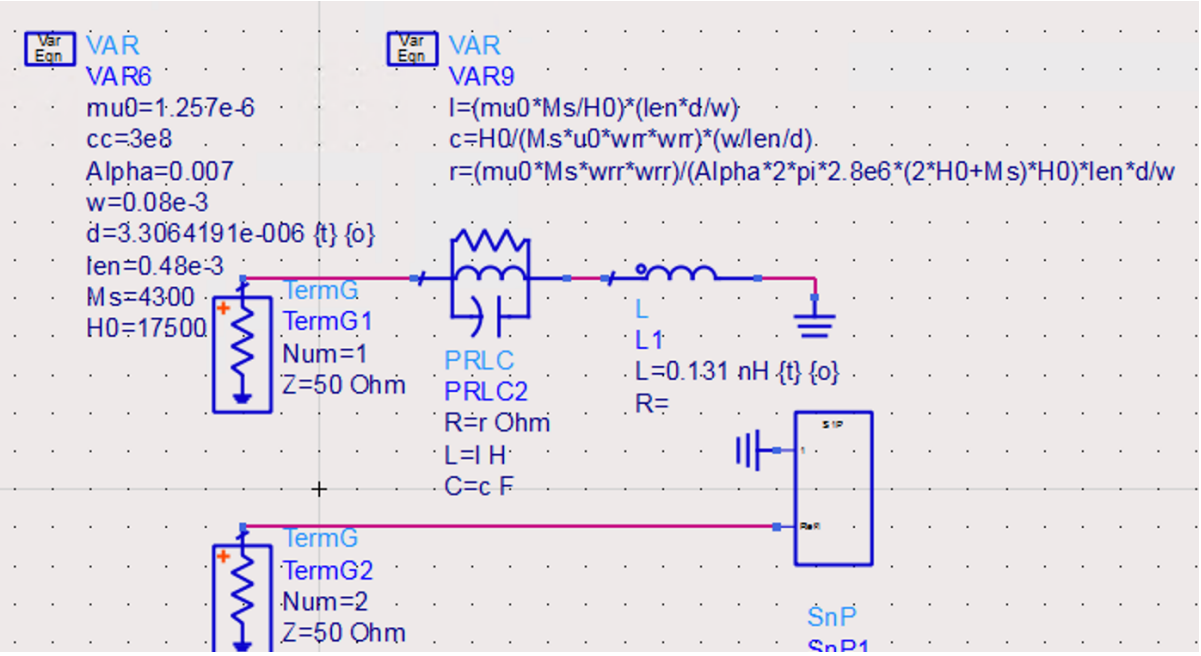

Figure 3.2.1: Simulation schematic in ADS to optimize the transmission line inductance and effective thickness of the ferrite material

The parameters used to construct the circuit model are those used in the full wave simulation like bias magnetic field strength, length, width of the transmission line, magnetic saturation of the ferrite material, etc. The r, l, c values are calculated from the equations (2.2.12) to (2.2.14). Specifically, a type of hexaferrite, B_aM is considered here, with $4\pi M_s = 4.3\ kG$ and damping constant $\alpha = 0.007$ (measured at 60 GHz). The addition of bias field and its internal anisotropy magnetic field is $17500\ Oe$, which gives the FMR frequency of 40 GHz:

$$\omega_r = \mu_0\gamma\sqrt{(H + H_a + (N_x - N_z)M_s)(H + H_a + (N_y - N_z)M_s)} \tag{3.2.1}$$

, where $N_x = 0,\ N_y = 0,\ N_z = 1$ when z is the thickness direction.

However, to get a close match between the HFSS results and ADS circuit model results, the thickness of the ferrite has to be optimized. This is because the previous derivation of ferrite resonator assumed

the magnetic spins inside the ferrite precess uniformly with the addition of external magnetic fields. Whereas in the actual device structure, the RF magnetic field provided by the stripline is not strictly uniform along the thickness direction of the ferrite. In other words, even though the actual thickness of the ferrite is 10 um, the effective thickness will be less than 10 um, when the length and width of the ferrite are chosen to be the same as transmission line length and width, respectively. In order to represent the active part of the ferrite material, the optimization tool in ADS is used, whose goals are to minimize the difference between HFSS results and ADS results by tuning the effective thickness of ferrite:

$$Goal\ 1 = \min\left(real(Z_{11}(HFSS)) - real(Z_{11}(ADS))\right) \tag{3.2.2}$$

$$Goal\ 2 = \min\left(imag(Z_{11}(HFSS)) - imag(Z_{11}(ADS))\right) \tag{3.2.3}$$

Figure 3.2.2 shows the comparison between HFSS results (blue curves) and ADS results (red curves) for both $real(Z_{11})$ and $imag(Z_{11})$. The close match between the two sets of results demonstrates the feasibility of the proposed circuit model.

Table 3.2.1 summarize the optimized parameters for different lengths of the transmission line structure. Since the constitution of bandpass filters require multiple resonators with different reactive components values, these parameters are saved for future reference to do the filter synthesis.

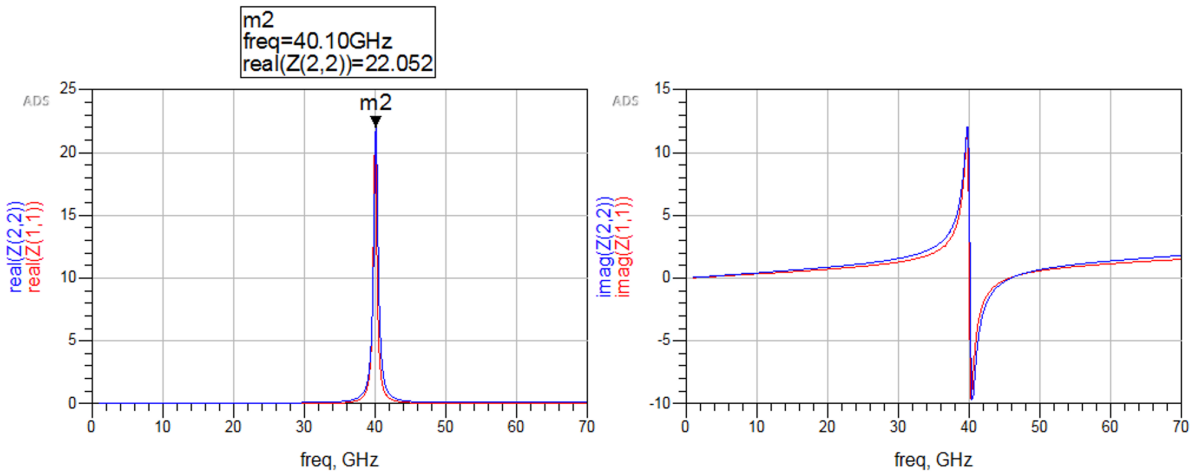

Figure 3.2.2: Comparison between HFSS results (blue curves) and ADS results (red curves)

Bias	H_ferrite	length	d_optimized	Lo(TL)	Lm	Cm	Rm
Ho+Ha= 17500 Oe	10um+10um (width=0.1mm)	0.1mm	3.4701517um	**0.0055 nH**	**1.5245 pH**	10.38 pF	27.07 Ohm
		0.12mm	3.591654um	**0.006 nH**	**1.8934 pH**	8.3572pF	33.62 Ohm
		0.144mm	3.591654um	**0.0075 nH**	**2.2563 pH**	7.0131 pF	40.06 Ohm
		0.16mm	3.591654um	**0.009 nH**	**2.5246 pH**	6.2679 pF	44.83 Ohm

Table 3.2.1: Summary of circuit parameters and optimization results

3.3 Bandpass Filter Synthesis and Simulation

There are several ways to do the filter design and synthesis. The insertion loss method, specifically, allows a high degree of control over the filter passband and stopband as well as the phase characteristics. Figure 3.3.1 illustrates the process of filter design with insertion loss method. The detailed procedure can be found in [4] and [6]. In this project, two kinds of bandpass filters are considered: bandpass filter using transmission line coupled resonators and bandpass filter using capacitively coupled resonators.

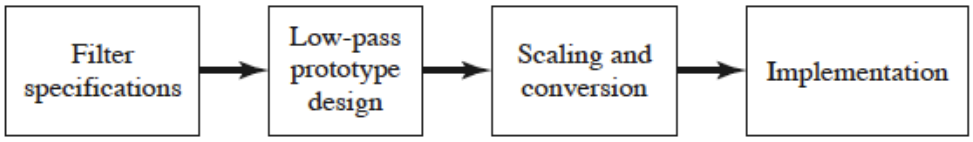

Figure 3.3.1: The process of filter design by the insertion loss method [4]

3.3.1 Bandpass Filter Using Transmission Line Coupled Resonators

In chapter 2.4, the filter structure using transmission line coupled resonators has been discussed briefly. Here we will extend this procedure and include simulation results. Figure 3.3.1.1 shows the synthesized filter parameters with 5% relative bandwidth at 40.05 GHz. The transfer response is set to be equal ripple. The L_1, L_2, L_3, C_1, C_2, C_3 values are calculated from (2.4.4). The coupling quarter wavelength transmission line has the characteristic impedance of 12.52 Ohm which is also the system reference impedance. The reason why the reference impedance is not the standard 50 Ohm is that it is affected by the ferrite resonators. With the current design structure, it's easier to synthesize the filter in lower impedances systems. Such limitations can be overcome when the physical dimension of the ferrite as well as the loading transmission line become more diverse.

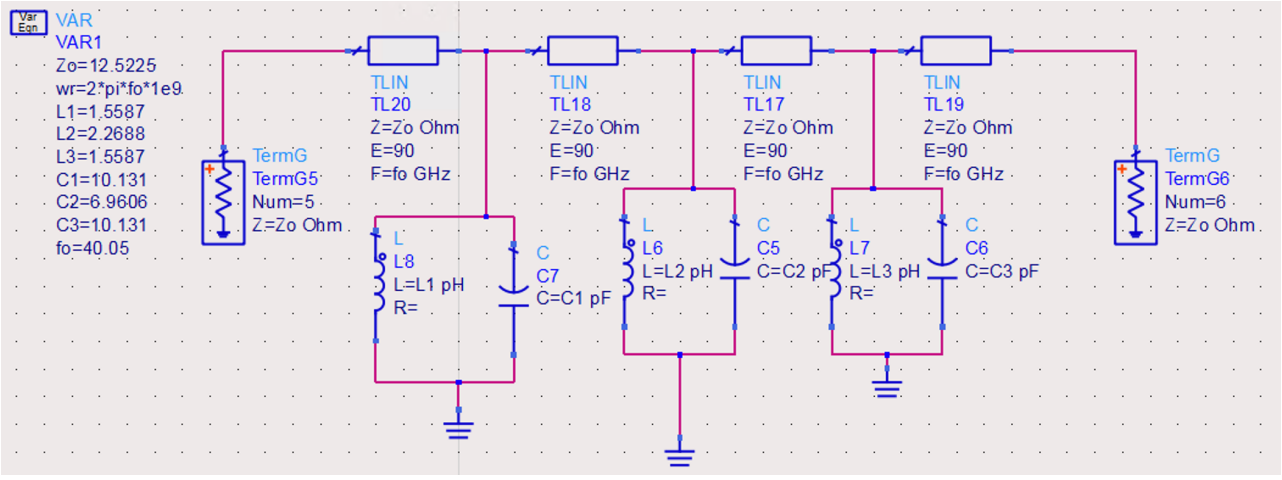

Figure 3.3.1.1: Original bandpass filter structure

Figure 3.3.1.2 extends from Figure 3.3.1.1 by replacing the ideal LC resonators with the actual RLC resonators where the resistance represents the loss in the ferrite material. Note that the RLC values are the optimized results as discussed previously. L_{o1}, L_{o2} and L_{o3} represents the transmission line inductances, which, when compared with Figure 3.3.1.1, are the parasitic that are not considered during filter synthesis. Hence, the series C_{o1}, C_{o2} and C_{o3} are added to counteract their effects by forming series resonances at FMR frequency which is also the filter center frequency.

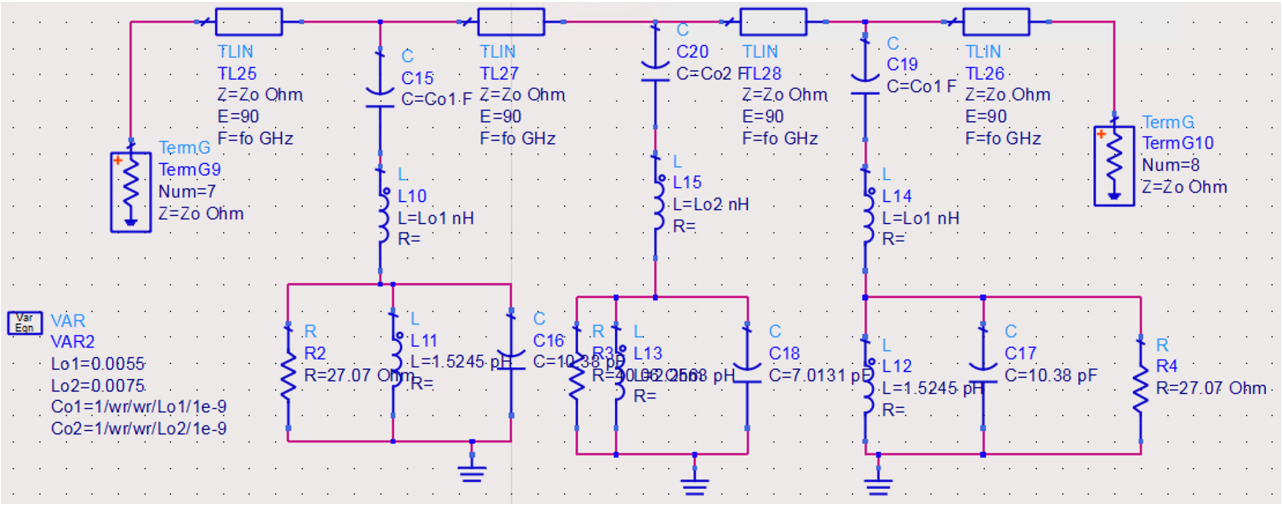

Figure 3.3.1.2: Bandpass filter structure with the equivalent circuit model of transmission line loaded ferrite resonators

In Figure 3.3.1.3, the equivalent circuits of transmission line loaded ferrite resonators are further replaced by the actual S parameter simulation results from HFSS. Generally, the three resonators should have different reactive components values to construct a 3rd order filter. However, since the equal ripple filter is considered here, the first and the third resonators are essentially the same, corresponding to the transmission line length of 0.1 mm (which is also the length of ferrite material). And the second SnP device corresponds to the S parameter simulated from the structure when the length of transmission line is 0.144 mm. Actually, after the optimization process to find the effective thickness of the ferrite material, the ferrite $\frac{w}{d\_eff}$ can be viewed as a constant. And the adjustment of

inductances and capacitances in ferrite resonators can be done easily by changing the length of ferrite, according to (2.2.12) to (2.2.14). This will make the filter synthesis following a systematic way.

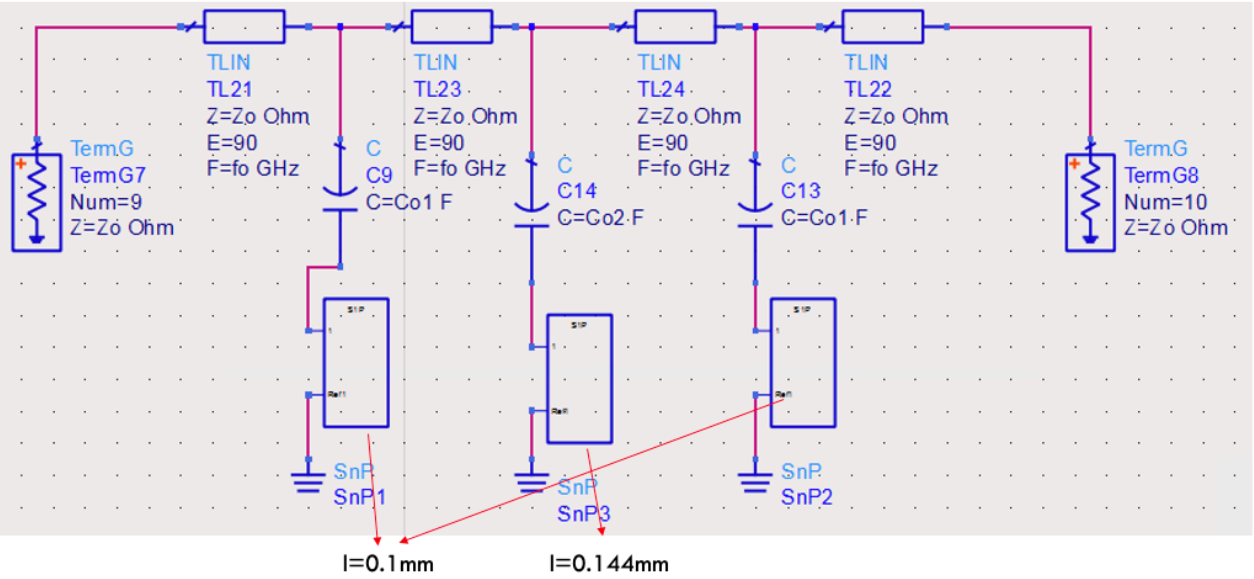

Figure 3.3.1.3: Bandpass filter structure with the SnP devices representing actual simulation results from HFSS

Figure 3.3.1.4 summarized the simulation results for the above three circuit schematics. The red curve represents the ideal filter response without any loss in passband. The blue curve is the filter response generated from the equivalent circuit model in Figure 3.3.1.2 and the pink curve is the filter response generated from HFSS S parameters. The filter center frequency is 40.05 GHz. This figure demonstrates the effectiveness of the proposed equivalent circuit model approach to synthesize the 3rd order bandpass filter. In addition, the close match between the pink curve and red curve indicates that the optimization is quite accurate. Compared with the ideal filter, the 5 dB in-band attenuation comes from the loss in the ferrite material. However, when the frequency is far away from the passband, the transmission characteristic will rise again due to the existence of transmission line inductances. The additional capacitors are only capable of eliminating their influence near the center

frequency. Of course, such phenomenon can be minimized by better transmission line design and using other methods to eliminate their effects.

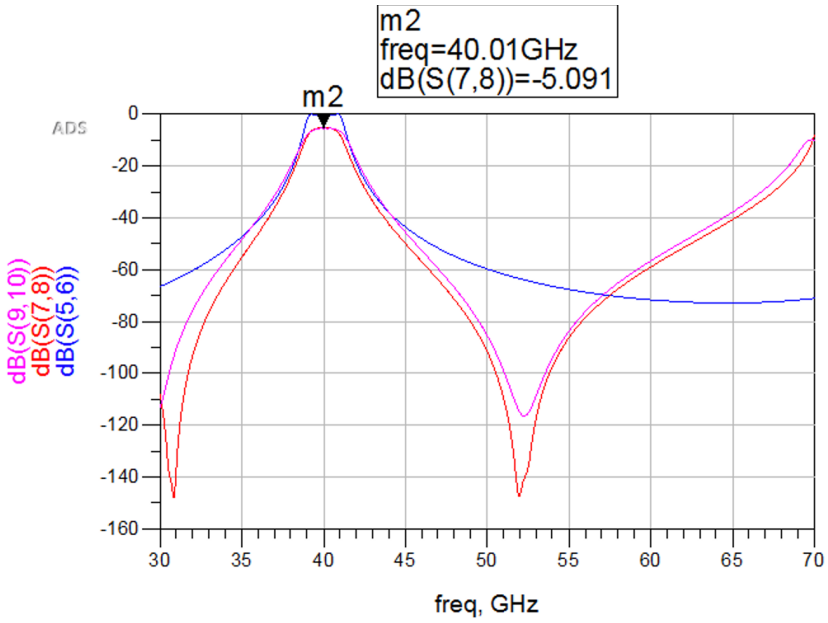

Figure 3.3.1.4: Simulation results: red curve: ideal filter response without loss in passband; Blue curve: filter response generated from the equivalent circuit model; Pink curve: filter response generated from HFSS s parameters

3.3.2 Bandpass Filter Using Capacitively Coupled Resonators

A related type of bandpass filter exploits capacitively coupled resonators and is often referred to as ceramic resonator filters when made from coaxial line with ceramic materials. The design procedure of such filters can be understood from Figure 3.3.2.1, which starts from the general bandpass filter schematic with admittance inverters, i.e., J_{01}, J_{12}, etc. In the previous structure, the admittance inverters are quarter wavelength transmission lines. Here, on the other hand, the admittance inverters are implemented with π networks. C_{12}, $(-C_{12})$, and $(-C_{12})$ are the example of one unit of π network. Note that even though the negative capacitances are used here, which, of course, don't exist in nature, they will be later absorbed by the rest of the circuits.

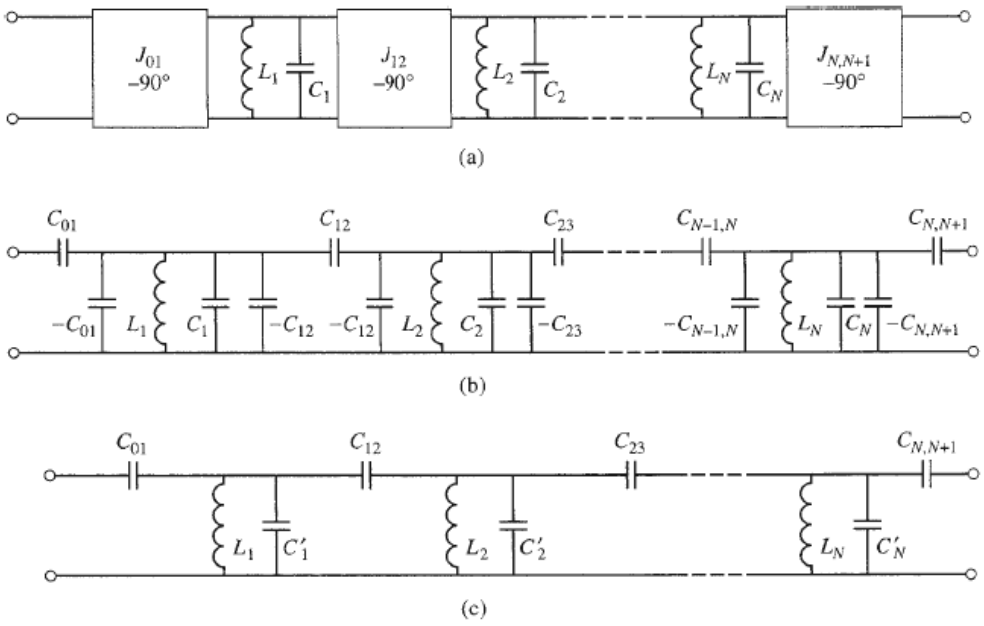

Figure 3.3.2.1: Equivalent circuit for the bandpass filter. (a) A general bandpass filter circuit using shunt resonators with admittance inverters. (b) Replacement of admittance inverters with the circuit implementation. (c) After combining shunt capacitor elements. [4]

Using the analysis in [4], the admittance inverter constants can be derived as:

$$Z_0 J_{01} = \sqrt{\frac{\pi\Delta}{4g_1}} \tag{3.3.2.1}$$

$$Z_0 J_{n,n+1} = \frac{\pi\Delta}{4\sqrt{g_n g_{n+1}}} \tag{3.3.2.2}$$

$$Z_0 J_{N,N+1} = \sqrt{\frac{\pi\Delta}{4g_N g_{N+1}}} \tag{3.3.2.3}$$

, where Δ is the relative bandwidth, g_n is the lowpass filter prototype constants and Z_0 is the reference impedance. Similarly, the coupling capacitor values in Figure 3.3.2.1 (b) can be found as:

$$C_{01} = \frac{J_{01}}{\omega_0\sqrt{1-(Z_0 J_{01})^2}} \tag{3.3.2.4}$$

$$C_{n,n+1} = \frac{J_{n,n+1}}{\omega_0} \tag{3.3.2.5}$$

$$C_{N,N+1} = \frac{J_{N,N+1}}{\omega_0\sqrt{1-(Z_0 J_{N,N+1})^2}} \tag{3.3.2.6}$$

Note that the end capacitors are treated differently than the internal elements.

Afterwards, the negative capacitors are combined with the larger capacitors in the LC resonators as shown in Figure 3.3.2.1 (c). Thus, the effective resonator capacitor values are given by:

$$C_n' = C_n + \Delta C_n = C_n - C_{n-1,n} - C_{n,n+1} \tag{3.3.2.7}$$

, where ΔC_n represents the change in the resonator capacitance caused by the parallel addition of the inverter elements.

Figure 3.3.2.2 shows the original filter schematic built directly from Figure 3.3.2.1 (b) with center frequency of 34.85 GHz, 5% relative bandwidth and equal ripple response. The lumped elements values are calculated from the equations above. Note that in this step, the transmission line inductances of ferrite resonators are not included.

Figure 3.3.2.3 extends from Figure 3.3.2.2 by adding transmission line inductances L_o and the corresponding resonate capacitance C_o. As before, the cancellation of L_o is only effect around the center frequency.

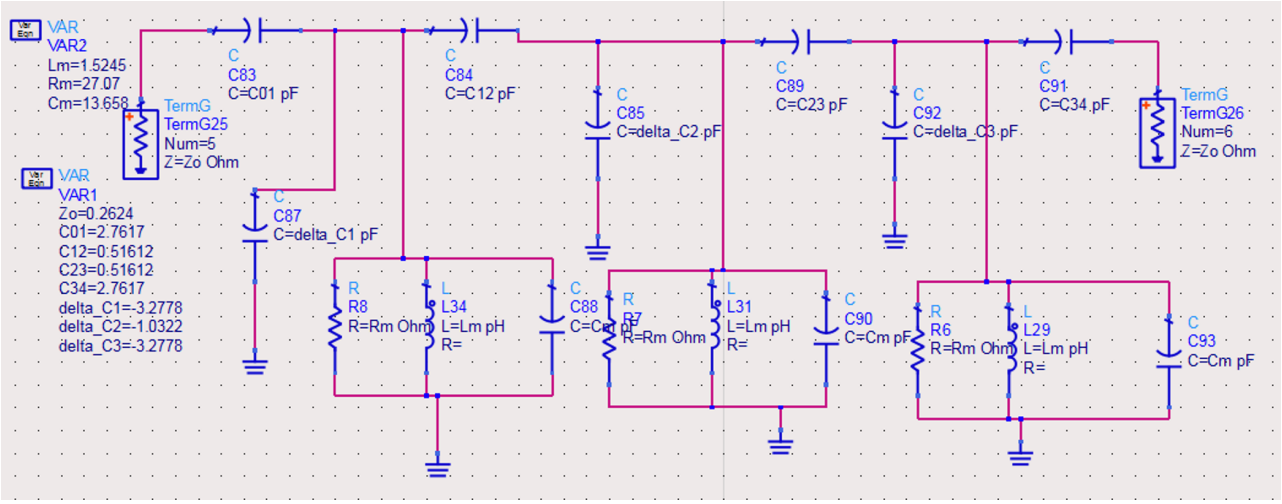

Figure 3.3.2.2: Original bandpass filter structure

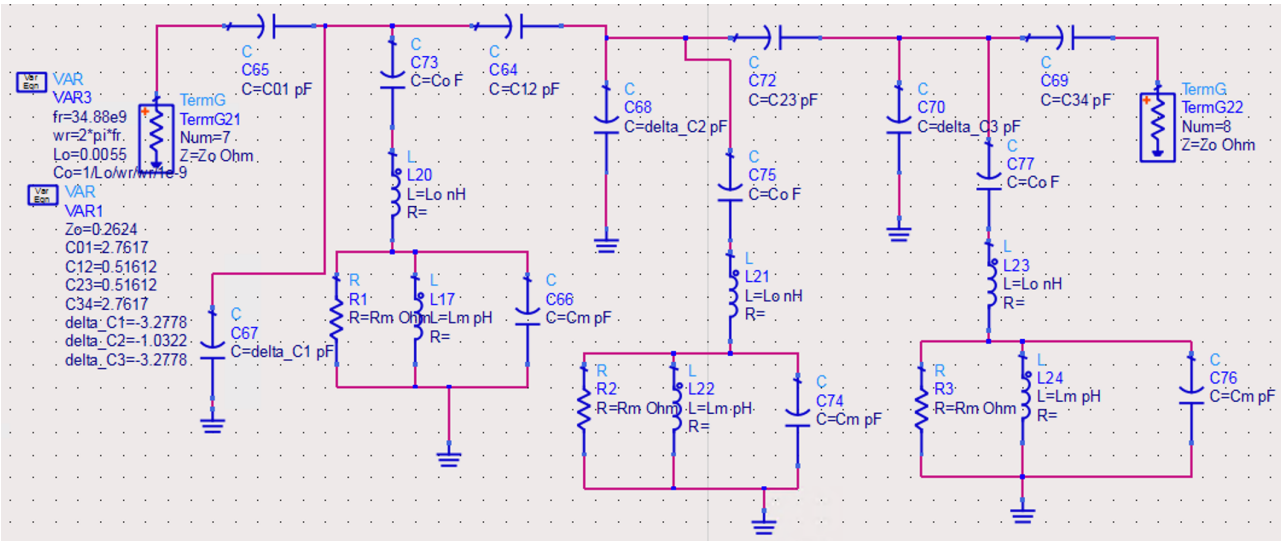

Figure 3.3.2.3: Bandpass filter structure with the equivalent circuit model of transmission line loaded ferrite resonators

Then, the problem arises as to how to absorb the negative capacitances into the rest of circuits. For this project, the negative capacitors $delta\_C_1$, $delta\_C_2$, and $delta\_C_3$ are combined directly with the ferrite capacitor C_m. This is not accurate, since the addition of transmission line inductances is not considered. However, there are other ways of integration such as the technique illustrated in [7], which may be the future research objective.

After absorbing the negative capacitances, the ferrites should resonate at higher frequencies than the filter operation (center) frequency. And since the $delta\_C_1$, $delta\_C_2$, and $delta\_C_3$ are not the same, the FMR frequencies for each ferrite resonators are different as well. Figure 3.3.2.4 shows the design parameters from HFSS, where the first and third resonators are biased at 984000 A/m while the second resonator is biased at 878500 A/m.

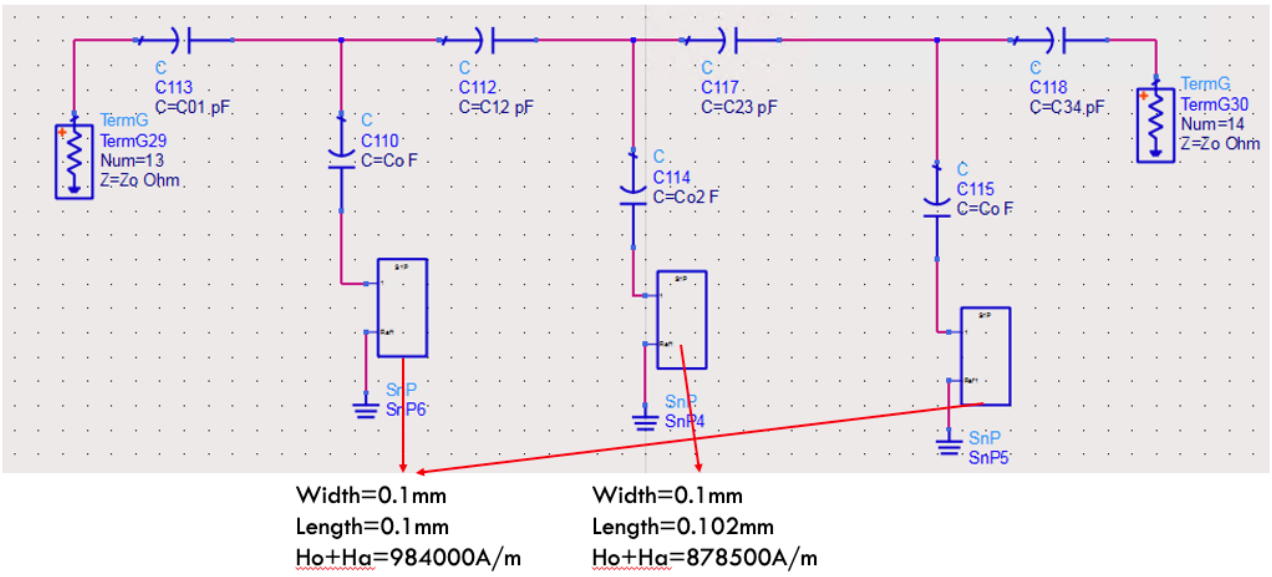

Figure 3.3.2.4: Bandpass filter structure with the SnP devices representing actual simulation results from HFSS

Figure 3.3.2.5 summarized the simulation results of filter transfer characteristics. The red curve is the original filter response (Figure 3.3.2.2). The blue curve is filter response generated from the equivalent circuit model in Figure 3.3.2.3 and the pink curve is the filter response generated from HFSS S parameters in Figure 3.3.2.4. The distortion of the pink curve is caused by the extra transmission line inductances.

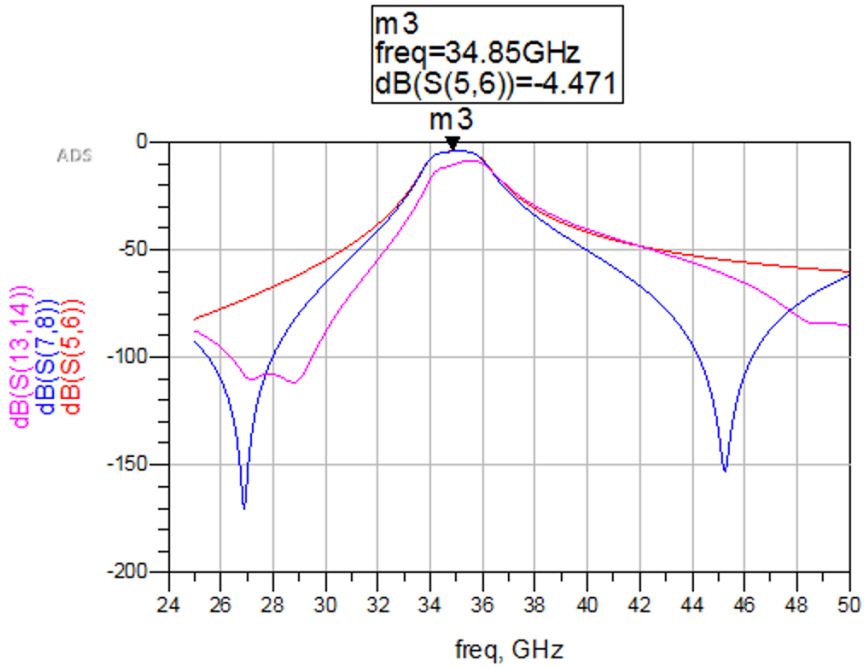

Figure 3.3.2.5: Simulation results: red curve: original filter response; Blue curve: filter response generated from the equivalent circuit model; Pink curve: filter response generated from HFSS s parameters

3.3.3 Summary and Comparison

Compared with the transmission line coupled filters, the capacitively coupled filters have the advantage that the filter relative bandwidth can be easily tuned by changing the coupling capacitances, as indicated in (3.3.2.4) to (3.3.2.6). However, the drawback is that the FMR frequency is different than the operation frequency for each unit of ferrite material, which may be hard to implement in reality.

Figure 3.3.3.1 summarized the filter center frequency tunability by changing the bias magnetic field strength. The filter structure is based on coupled transmission lines.

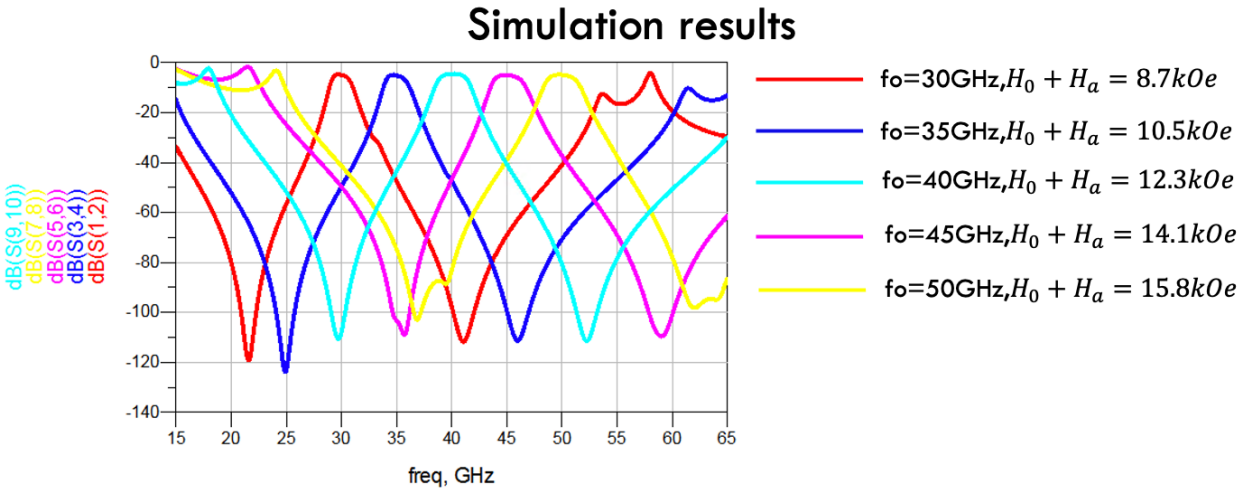

Figure 3.3.3.1: Summary of filter tunability

CHAPTER 4

Design Considerations and Discussion on Physical Parameters

In this Chapter, several design considerations are taken into account and the effects of them on the filter characteristics are included. First of all, the internal anisotropy of the specific kind of ferrimagnetic material, hexaferrite is illustrated, which makes it possible to raise FMR frequency to millimeter wave band and facilitate filter design at higher frequencies. Afterwards, the effects of ferrite thickness, transmission line structures and conductor widths are included. In the HFSS device layout and in actual experiment, these are important parameters to optimize. To conclude, stripline structure sandwiched with ferrites less than 20 um thick is suitable to excite FMR mode.

4.1 Effect of Ferrimagnetic Material Anisotropy

As stated in Chapter 2 and Chapter 3, the internal anisotropy field inside some kinds of ferrite material is capable of increasing the FMR frequency without the need to apply extremely large static magnetic bias field, i.e., up to 10 KOe, which requires large permanent magnets. In fact, depending on the magnetization direction relative to the principal axes of the crystal, an additional energy, anisotropy energy, may be present in ferrimagnetic crystals [11][12]. Such anisotropy magnetic field will add additional torque on the magnetic spin:

$$\overrightarrow{T_a} = \mu_0 \vec{M} \times \overrightarrow{H_a} \tag{4.1.1}$$

, where H_a is the effective anisotropy field. As a result, the resonance condition is modified by this magnetic anisotropy field and is given by (3.2.1): $\omega_r = \mu_0\gamma\sqrt{(H + H_a + (N_x - N_z)M_s)(H + H_a + (N_y - N_z)M_s)}$.

An important observation is that ferromagnetic resonance can be observed in ferrites having nonzero anisotropy even if there is no external magnetic bias field, which is the self-bias phenomenon.

Generally speaking, microwave ferrites refer to the entire family of iron oxides which include spinels, garnets, hexaferrites, and orthoferrites, as presented in Table 4.1.1. Specifically, hexagonal ferrites, or hexaferrites, usually have larger magnetic anisotropy field strength H_a compared with spinel ferrite and garnet ferrite. And many attempts have been made to improve the magnetic properties of hexaferrites by doping and substitutions within their complex structure. The M-type hexaferrite, i.e., $B_a Fe_{12} O_{19}$, or $B_a M$ in short, have been exploited in various applications such as permanent magnets, plastoferrites, injection-molded pieces, microwave devices, and magnetic recording media [12][13]. The previous discussions in Chapter 2 and 3 are also based on $B_a M$ ferrite with magnetic anisotropy field of 17 KOe, magnetization saturation of 4300 Gauss and damping constant 0.007 measure at 60 GHz [2].

However, it is worth noticing that the proposed equivalent circuit models for transmission line loaded ferrite materials and the corresponding filter circuits are not limited to hexaferrite or any particular type of ferrite. In fact, the anisotropy field can be viewed as the addition to static magnetic bias field during the simulation in HFSS. And different material properties can be adjusted accordingly to get a best representation of the experimental results.

	Material	Abbreviation	T_N (°C)	Landé g-factor	$4\pi M_s$ (Gauss)	Magnetic anisotropy H_a (Oe)	Coercive field H_c (Oe)
Hexaferrite	$BaFe_{12}O_{19}$	BaM	450	1.87	4,000	17,460	1,935
	$SrFe_{12}O_{19}$	SrM	455		4,320	16,000	6,635
	$Ba_4Zn_2Fe_{36}O_{60}$	Zn_2U	400		4,223	10,038	2,580
	$Ba_2Co_2Fe_{28}O_{46}$	Co_2X	467		3,400	9,500	50
	$Ba_2MnZnFe_{12}O_{22}$	MnZnY	100		2,300	9,500	60
	$BaZn_2Fe_{16}O_{27}$	Zn_2 W			4,950	12,000	184
	$BaCo_2Fe_{16}O_{27}$	Co_2 W	430	1.90	4,800	21,000	80
	$Ba_3Co_2Fe_{24}O_{41}$	Co_2Z	400		3,300	12,000	23
	$Ba_3Zn_2Fe_{24}O_{41}$	Zn_2Z			3,900	4,810	
Spinel	$MgFe_2O_4$	MgFO	320[a]	2.06	2,150[a]	173	1.8[a]
	$MnFe_2O_4$	MnFO	340	2.20	4,000	5,400	196
	$Li_{0.2}Zn_{0.6}$ $Fe_{2.2}O_4$		277	2.08	2,730	7,330	
	$CoFe_2O_4$	CFO	520		5,370	6,800	1,566
							2,720
	$NiFe_2O_4$	NFO	585[a]	2.4	3,000[a]	425	5.7[a]
Garnet	$Y_3Fe_5O_{12}$	YIG	280	2.00	1,750	82	
	$Y_3Fe_{5-x}Ga_x$ O_{12}	GaYIG	167	2.03	400		

Table 4.1.1: Crystal and physical properties of some ferrites [11]

4.2 Effect of Ferrite Thickness

As discussed in Chapter 2, the FMR frequency is affected by the ferrite dimensions and the demagnetization factors in x, y, z directions. The general equation to calculate FMR frequency is given by (4.2.1), and Figure 4.2.1 illustrates the relation between f_r and N_z when z is the thickness direction and $N_x = N_y = \frac{1-N_z}{2}$. From the plot, it's obvious that with N_z decreasing, the theoretical FMR frequency will decrease. However, the previous discussion in Chapter 2 to derive the equivalent impedances of ferrite resonator is based on the assumption that $N_z = 1$, and (4.2.1) will reduce to (4.2.2) since $N_x = N_y = 0$.

As a result, to satisfy such assumption, the thickness of the ferrite in the actual physical model can't be too large. Actually, simulation results of resonant frequencies versus different ferrite thickness indicate that such assumption will hold valid as long as the ferrite is equal to or less than 20 um thick.

Given that design constraint, the corresponding thickness can be optimized as discussed in Chapter 3.

$$\omega_r = \mu_0\gamma\sqrt{(H + H_a + (N_z - N_x)M_s)(H + H_a + (N_y - N_x)M_s)} \quad (4.2.1)$$

$$\omega_r(thin\ film) = \mu_0\gamma\sqrt{(H + H_a + M_s)(H + H_a)} \quad (4.2.2)$$

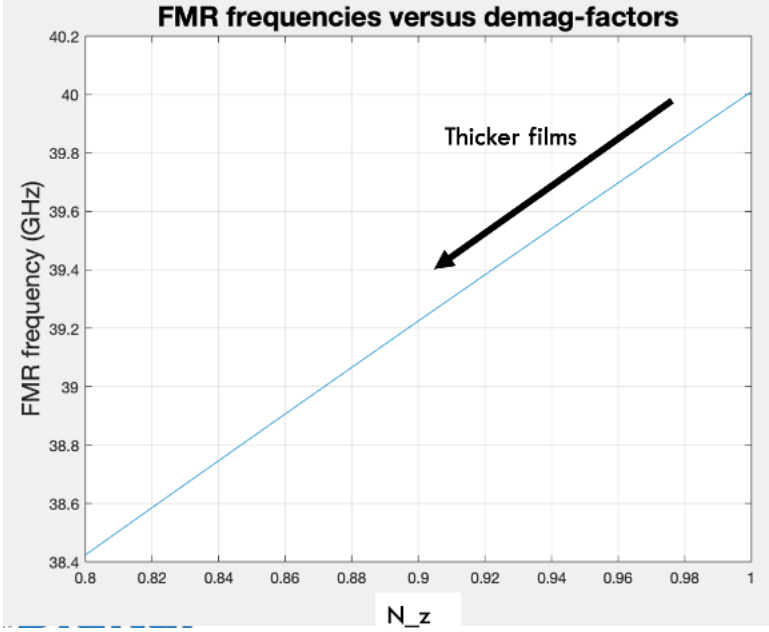

Figure 4.2.1: Theoretical FMR frequency versus demagnetization factor in z (thickness) direction

4.3 Effect of Transmission Line Structure

The FMR can be viewed as the lowest order of spin wave when all the magnetic spin unit inside the ferrite material precess uniformly around the static magnetic field bias direction at the frequency dominated by the RF magnetic field. Apart from the FMR mode, multiple spin wave modes can propagate inside the ferrite material like magnetostatic modes and exchange dominated spin wave modes [8]. The former can be viewed as electromagnetic waves affected by the permeability tensor during propagation in the ferrite material. And numerous non-reciprocal devices have been made by

virtue of the nature of anisotropy and non-reciprocal properties of the ferrite material, such as magnetic circulators [9][10]. The latter, on the other hand, becomes dominate when the propagation constant k of the spin waves becomes larger, typically in the range of $10^7 \sim 10^8/m$. The large k corresponds to smaller wavelength compared with the ferrite material dimension, indicating that the magnetic spins will no longer precess uniformly and in phase within the material. The exchange magnetic field between neighboring spins can be quantitively described by the exchange coefficient, usually referred by λ_{ex}. Such mechanism can be incorporated into our existing equivalent circuit model by adding exchange inductors between the neighboring RLC resonators to recover the original spin wave dispersion curve. The detailed analysis is included in the paper [1].

Hence, due to the complexity and diversity of spin wave modes, it is critical to ensure that the FMR mode is excited rather than other modes that are not represented using the circuit model. And that requires the proper selection of transmission line structure to provide uniform RF magnetic field to the ferrite material. Figure 4.3.1 shows the comparison between the electric field lines for both microstrip line and stripline structure in HFSS. When the center conductor is sandwiched by two pieces of ferrite materials, the stripline structure is more desirable, because there are two grounds placed on top and bottom side. As a result, the two ferrite films are excited simultaneously and uniformly. In fact, the stripline structure has been exploited in experiment in [2] to excite the FMR mode successfully.

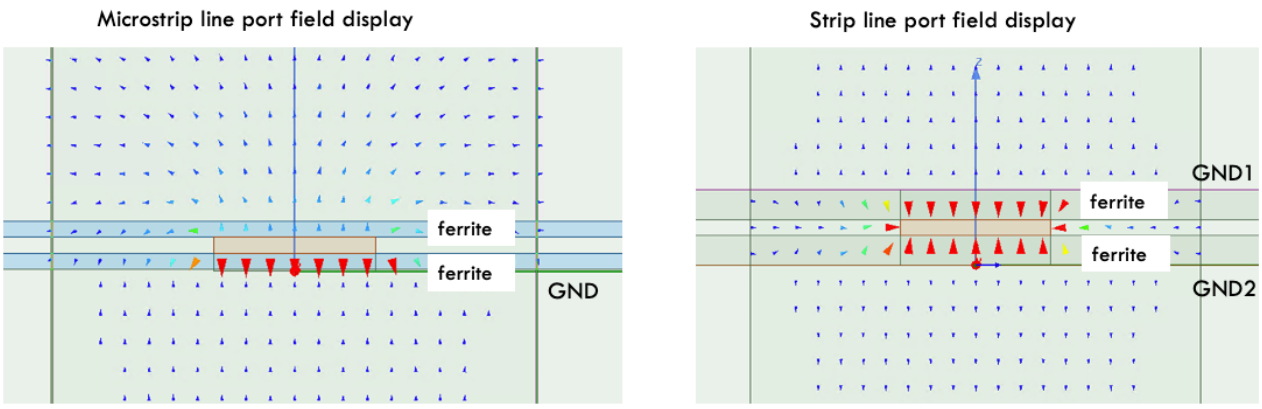

Figure 4.3.1: Electric field strength line visualization for microstrip line and stripline structure in HFSS

Figure 4.3.2 and Figure 4.3.3 further confirm the advantage of stripline structure by comparing the optimization results of the input impedances. For both cases, the red lines represent the real parts and imaginary parts of the input impedances obtained from our proposed equivalent circuit models. The blue curves in Figure 4.3.2 represent the HFSS simulation results for microstrip line structure. It's obvious that at the frequencies higher than 40 GHz, there remain some discrepancies of the two sets of results. And this is due to higher order spin wave modes at higher than FMR frequency range that are not predicted by the circuit model. Compared with microstrip line case, Figure 4.3.3 has a much better fit, indicating that the stripline structure is more suitable to generate FMR mode. And the previous filter simulation results are also generated with stripline structure.

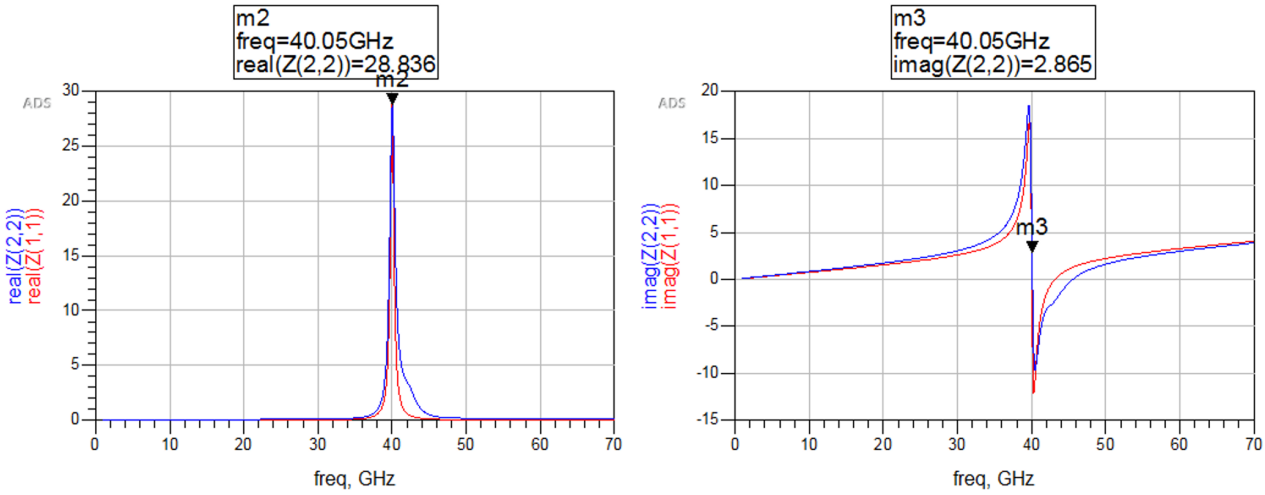

Figure 4.3.2: Optimization results for input impedances. The red curves represent the circuit model results and the blue curves represent the HFSS results for microstrip line structure

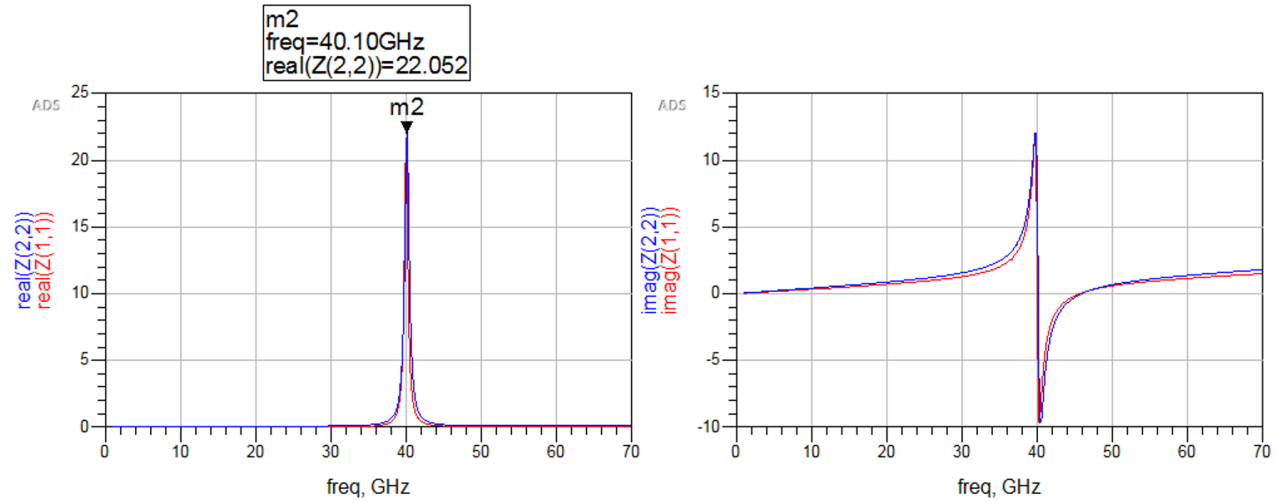

Figure 4.3.3: Optimization results for input impedances. The red curves represent the circuit model results and the blue curves represent the HFSS results for stripline structure

Apart from microstrip line and stripline structure, co-planer waveguide (CPW) structure has also been experimented. However, the intrinsic nonuniform field distribution of CPW line is not suitable to excite FMR mode as well. In fact, paper [3] utilized CPW structure to excite confined magnetostatic waves.

4.4 Effect of Conductor Width

The conductor width will affect the characteristic impedances of the transmission line structures and the corresponding transmission line inductance. And it will also change the ferrite inductance according to equation (2.2.13). To achieve the maximum ratio of ferrite inductance versus TL inductance, i.e., $\frac{L_m}{L_0}$, the conductor widths are swept from $0.08\ mm$ to $0.18\ mm$, as shown in Figure 4.4.1. The width of $0.1\ mm$ will give the highest $\frac{L_m}{L_0}$ ratio and is thus adopted in the previous simulation parameter setups. Note that even at this point, the ferrite inductance is smaller than transmission line inductance because of the high operation frequency that increase ω_o on the denominator of the L_m expression. This also explains the reason why the transmission line inductances will have such large effect on the final filter response.

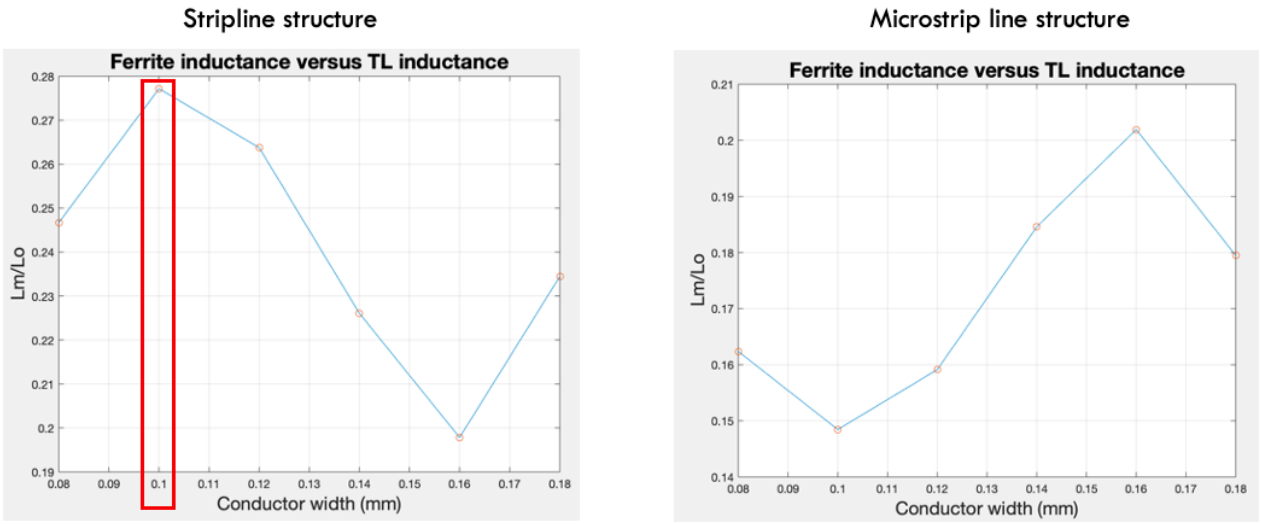

Figure 4.4.1: The relation between $\frac{L_m}{L_o}$ versus different conductor widths for stripline structure (left) and microstrip line structure (right)

CHAPTER 5

Conclusion and Future Work

In conclusion, this work proposed an equivalent circuit model for tunable band pass filters based on ferromagnetic resonance, which is used to synthesize the 3rd order band pass filters. In addition, the full wave simulation results match with the results obtained from the equivalent circuit model, which provide a validation to the operating principle of the proposed bandpass filter. The hexaferrite is considered in the simulation, whose internal magnetic anisotropy field is able to increase the FMR frequency as well as the filter operation frequency up to millimeter wave range. Having said that, the proposed circuit model is not restricted to hexaferrite, but can be generalized to any type of thin film ferrite material with the known magnetization saturation, damping constant and physical dimensions. In fact, the high operation frequency will make it obvious the transmission line inductances, whose effects need to be minimized by better circuit design.

In this work, the operation frequency range of this circuit model is around 30 GHz to 50 GHz. Further increase in the operation frequency will need larger magnetic bias field. In addition, the lumped circuit model for stripline will become less accurate when the electromagnetic wave wavelength becomes shorter compared with the actual length of stripline. In such case, a single inductor is not sufficient to represent the transmission line unit and multiple sections of LC ladder networks are needed. Theoretical derivation of the distributed lumped element values can be found in [19]. Another consideration of transmission line modeling at higher frequencies is that the radiation effect may become obvious so that there will be radiation resistance associated with circuit models.

Future work includes modeling the internal nonlinearity of ferrimagnetic materials to predict large signal behavior, since the power handling of the ferrite-based filters have been a bottleneck for

research. In addition, apart from the FMR mode, the spin wave propagation in ferrites need a proper circuit modeling when the excitation becomes nonuniform. That is to say, the spin units are no longer precessing uniformly within the medium, and there will be exchange coupling between neighboring spins. Such coupling will enable the spin wave propagation frequency higher than the FMR frequency, which is the exchange spin waves. And the magnetostatic waves, which is another kind of spin wave, may be represented by the circuit models as well to give a better fit to the full wave simulation results.

REFERENCES

[1] H. Cui, Z. Yao and Y. E. Wang, "Coupling Electromagnetic Waves to Spin Waves: A Physics-Based Nonlinear Circuit Model for Frequency-Selective Limiters," IEEE Transactions on Microwave Theory and Techniques, vol. 67, no. 8, pp. 3221-3229, Aug. 2019, doi: 10.1109/TMTT.2019.2918517.

[2] Song, Young-Yeal, César L. Ordóñez-Romero, and Mingzhong Wu. "Millimeter wave notch filters based on ferromagnetic resonance in hexagonal barium ferrites." Applied Physics Letters 95.14 (2009): 142506.

[3] Lu, Lei, et al. "Planar millimeter wave band-stop filters based on the excitation of confined magnetostatic waves in barium hexagonal ferrite thin film strips." Applied Physics Letters 98.21 (2011): 212502.

[4] Pozar, David M. Microwave engineering. John wiley & sons, 2011.

[5] Lax, Benjamin, Kenneth J. Button, and H. J. Hagger. "Microwave ferrites and ferrimagnetics." Physics Today 16.8 (1963): 57.

[6] Matthaei, G. L., Leo Young, and E. M. Jones. Design of Microwave Filters, Impedance-Matching Networks, and Coupling Structures. Volume 2. Stanford Research Inst Menlo Park CA, 1963.

[7] Wing-Yan Leung, K. -. M. Cheng and Ke-Li Wu, "Multilayer LTCC bandpass filter design with enhanced stopband characteristics," in IEEE Microwave and Wireless Components Letters, vol. 12, no. 7, pp. 240-242, July 2002, doi: 10.1109/LMWC.2002.801130.

[8] Stancil, Daniel D., and Anil Prabhakar. Spin waves. Vol. 5. New York: Springer, 2009.

[9] Saib, Aimad, et al. "An unbiased integrated microstrip circulator based on magnetic nanowired substrate." IEEE transactions on microwave theory and techniques 53.6 (2005): 2043-2049.

[10] Śmigaj, Wojciech, et al. "Magneto-optical circulator designed for operation in a uniform external magnetic field." Optics letters 35.4 (2010): 568-570.

[11] Özgür, Ümit, Yahya Alivov, and Hadis Morkoç. "Microwave ferrites, part 1: fundamental properties." Journal of Materials Science: Materials in Electronics 20.9 (2009): 789-834.

[12] Pullar, Robert C. "Hexagonal ferrites: a review of the synthesis, properties and applications of hexaferrite ceramics." Progress in Materials Science 57.7 (2012): 1191-1334.

[13] P.B. Braun, Nature 170, 708 (1952). doi:10.1038/170708a0

[14] Kabos, Pavel, and V. S. Stalmachov. Magnetostatic Waves and Their Application. Springer Science & Business Media, 2012.

[15] Adam, J. Douglas, et al. "Ferrite devices and materials." IEEE Transactions on Microwave Theory and Techniques 50.3 (2002): 721-737.

[16] https://en.wikipedia.org/wiki/Curie_temperature

[17] Gu W. Ferromagnetic resonance enhanced electrically small antennas. [Order No. 27666778]. University of California, Los Angeles; 2019.

[18] Lecture notes, UCLA ECE 163A “Introductory Microwave Circuits”.

[19] F. Schnieder and W. Heinrich, "Model of thin-film microstrip line for circuit design," in IEEE Transactions on Microwave Theory and Techniques, vol. 49, no. 1, pp. 104-110, Jan. 2001, doi: 10.1109/22.899967.